Additive Manufacturing 116 (2026) 105079

Contents lists available at ScienceDirect

Additive Manufacturing

journal homepage: www.elsevier.com/locate/addma

Formation of compositionally graded grains and molten-salt corrosion behavior in wire-arc additive manufactured NiMoCr alloy-cladded steel

Hanliang Zhu [a,b,*], Zhijun Qiu [a,b], Zhiyang Wang [a], Ondrej Muránsky [a], Inna Karatchevtseva [a], Huijun Li [b]

[a] Australian Nuclear Science and Technology Organisation (ANSTO), Lucas Heights, NSW 2234, Australia
[b] School of Mechanical, Materials, Mechatronic and Biomedical Engineering, University of Wollongong, Northfields Avenue, Wollongong, NSW 2522, Australia

ARTICLE INFO

Keywords:
Wire-arc additive manufacturing
NiMoCr alloy cladded 316 L stainless steel
Microstructure
Fluoride molten salt corrosion
Microstructural evolution

ABSTRACT

A nickel-based alloy containing Mo and Cr as the primary alloying elements (NiMoCr) was deposited onto 316 L stainless steel via wire-arc additive manufacturing (WAAM), and its microstructural evolution and high-temperature corrosion behavior in molten FLiNaK salt at 750 °C were investigated. The as-deposited cladding exhibited a highly textured dendritic γ-Ni matrix with significant Mo segregation and minor carbide formation in interdendritic regions. At the cladding-substrate interface, compositionally graded grains (CGGs) developed across a transition zone, displaying smooth chemical and crystallographic continuity without a distinct boundary. Corrosion testing for 500 h revealed corrosion rates of 0.11 mm/year for the NiMoCr cladding, 0.29 mm/year for the steel substrate, and 0.18 mm/year for the bistructure, indicating a gradient in corrosion resistance across the system. Post-exposure analysis and thermodynamic modelling showed that the steel substrate underwent intergranular corrosion, driven by rapid Cr diffusion and depletion along grain boundaries, further accelerated by galvanic coupling with the NiMoCr cladding. In contrast, Mo segregation in the NiMoCr alloy suppressed Cr diffusion and promoted the dynamic formation of corrosion-resistant σ-phase precipitates. These precipitates, along with the surrounding Mo-enriched matrix, mitigated galvanic interactions and shifted the dominant corrosion mode from interdendritic to intradendritic. Moreover, the CGGs helped maintain interface integrity by forming a transition zone that did not undergo preferential degradation.

1. Introduction

The molten salt reactor (MSR) is one of the six reactor technologies selected by the Generation IV International Forum for continued research and development [1]. As a promising candidate for small modular reactors (SMRs) deployment, the MSR offers distinct advantages over conventional light water reactors in terms of safety, environment impact, economic viability, and proliferation resistance [2]. MSRs utilize a circulating liquid fuel system in which fissile materials are dissolved in a molten salt carrier, enabling efficient heat transfer between the reactor core and external heat exchangers [1]. Unlike traditional reactors, MSRs operate at near-atmospheric pressures, significantly reducing mechanical stresses on structural components and enhancing overall safety [3,4]. However, the elevated operating temperatures (typically 700–800 °C) and the aggressive chemical nature of molten salts present subatantial challenges to the corrosion resistance of structural materials [4,5].

Nickel-based alloys containing Mo and Cr as the primary alloying elements have demonstrated superior corrosion resistance in molten fluoride salts, and are thus considered prime candidates for structural applications in MSRs [6–10]. Among them, Hastelloy-N, specifically developed for MSR environments, has been extensively studied. However, it suffers from limitations such as poor high-temperature creep strength and grain boundary embrittlement, preventing its certification for nuclear use [11]. Despite ongoing efforts to improve Hastelloy-N and develop its variants [11,12], the timeline for new alloy qualification remains long. In the interim, 316 stainless steels offer a viable option due to their ASME code certification, favorable mechanical properties and cost-effectiveness [13], though they lack sufficient corrosion resistance in molten salt environments [14]. A practical compromise is the use of Ni-based alloy cladding on stainless steel substrates, combining the corrosion resistance of Ni alloys with the mechanical robustness and affordability of stainless steels [15,16].

Several fabrication techniques have been applied to produce Ni alloy

* Corresponding author at: Australian Nuclear Science and Technology Organisation (ANSTO), Lucas Heights, NSW 2234, Australia.
E-mail addresses: hanliang.zhu@ansto.gov.au, hanliang_zhu@uow.edu.au (H. Zhu).

https://doi.org/10.1016/j.addma.2026.105079
Received 5 June 2025; Received in revised form 28 November 2025; Accepted 4 January 2026
Available online 5 January 2026
2214-8604/© 2026 The Author(s). Published by Elsevier B.V. This is an open access article under the CC BY license (http://creativecommons.org/licenses/by/4.0/).

cladded steels, with their microstructures and properties extensively investigated. Ferreira et al [17]. deposited Hastelloy C276 onto 316 L and API 5 L X70 steel using plasma transfer arc welding and reported a significant hardness drop at the interface due to carbide depletion and Fe enrichment. Morell-Pacheco et al [15]. examined Ni coated 316 L fabricated via cage plasma treatment and observed a high density of precipitates at the interface, contrasting with the relatively precipitate-free bulk alloy. They also reported increased swelling under Fe ion irradiation from cladding to substrate, suggesting improved radiation tolerance. Chen et al [18]. applied Inconel 718 onto 316 H via laser powder bed fusion. The microstructural analysis revealed chemical inhomogeneity, incomplete mixing, and Laves phase formation in the cladding, all contributing to a hardened interface region. These findings underscores that the interface in Ni alloy/steel bistructures often exhibits distinct microstructural and property characteristics from the substrate and cladding, which can impact their thermal stability, performance, and overall service reliability.

Wire-arc additive manufacturing (WAAM) has recently emerged as a cost-effective and scalable additive manufacturing technique that enables precise control over feedstock and thermal profiles. Its inherent layer-by-layer flexibility allows for controlled compositional transitions and customized microstructures. Compared with conventional coating techniques such as thermal spraying and physical vapor deposition (PVD), WAAM provides a fully metallurgical bond with low porosity and tunable thickness, which is essential for achieving durable protection under molten salt corrosion conditions [16,19–26]. Although WAAM is relatively slow and less adaptable to complex shapes, its capability to produce thick, defect-free, and compositionally graded claddings makes it particularly suitable for large-scale SMR components [16,19,20,23–26]. In our previous work, WAAM was used to deposit Hastelloy C276 Ni alloy onto P91 steel, achieving sound metallurgical bonding [16]. However, a sharp interface formed due to microstructural disparity, and the hardness in the transition zone nearly doubled that of both the cladding and substrate. In contrast, the present study employs WAAM to fabricate a NiMoCr alloy cladding on 316 L steel substrate aiming to achieve a more gradual transition in microstructure and corrosion properties.

The corrosion behavior of both stainless steels and Ni-based alloys in molten salts has been widely studied [4,6,9,10,27–32]. Doniger et al [30]. examined 316 L and 316 H in FLiNaK at 700 °C and observed Cr dissolution at grain boundaries and within grains, influenced by the choice of test capsule materials. Ouyang et al [4]. showed that moisture content exacerbates intergranular corrosion in Ni alloys due to carbide precipitation near grain boundaries. Gu et al [31]. reported stress-assisted Cr diffusion and carbide precipitation along grain boundaries, thereby forming a corrosion couple between the carbide and the matrix, facilitating the propogation of intergranular corrosion cracks into the grains in Hastelloy-N. Yin et al [10]. observed predominantly intergranular corrosion in 316 L, while Hastelloy-N exhibited both intergranular and pitting corrosion, with CrF_3 additions accelerating degradation. Graphite crucibles were considered to promote carbide formation near the grain boundary region of 316 L, leading to selective corrosion in this area. Sun et al [32]. studied 316L-Hastelloy-N couples in FLiNaK and identified galvanic interactions that enhanced Fe dissolution from 316 L. Meanwhile, Weinstein et al [11]. demonstrated that electroplated Ni claddings on 316 H protected Cr from leaching into molten FLiNaK. Collectively, these studies emphasize intergranular corrosion as a primary degradation mechanism for both stainless steels and Ni-based alloys exposed to molten fluoride salts. The preferential accumulation of cathodic precipitates at grain boundaries and the depletion of alloying elements along these boundaries are key mechanisms driving intergranular corrosion [4,10,31,33].

While the corrosion behavior of conventionally processed alloys has been extensively investigated, the performance of WAAM-fabricated Ni-based alloys and cladded steels in molten salt environments remain largely unexplored. The WAAM process involves high thermal gradients, rapid solidification, and repeated thermal cycles, which result in distinct microstructural features [25,34] that can significantly influence corrosion behavior compared to traditionally processed materials. This study systematically examines the microstructural evolution and high-temperature molten-salt corrosion behavior of WAAM-fabricated NiMoCr alloy cladded 316 L stainless steel in FLiNaK at 750 °C. Advanced microstructural characterization techniques, including SEM, EBSD, TEM, and thermodynamic modeling with Thermo-Calc [35] are employed to analyze both the as-deposited microstructure and its evolution following corrosion exposure. The findings provide valuable insights into the corrosion mechanisms affecting the NiMoCr cladding, steel substrate, and their interface region, offering critical guidance for the application of WAAM cladded structures in next-generation MSR systems.

2. Materials and methods

2.1. Materials fabrication

A NiMoCr alloy wire (3.0 mm diameter) was deposited onto a 316 L substrate using a WAAM system in a layer-by-layer manner. Before the WAAM deposition, the substrate surface was mechanically polished to expose a fresh surface and ensure good metallurgical bonding. The WAAM system comprises a gas tungsten arc welding power source, wire feeder, control and cooling systems, and a traveling stage. The chemical compositions of the NiMoCr wire and 316 L substrate are listed in Table 1.

Deposition was performed under fixed processing conditions: an arc current of 140 A, a voltage of 13.0 V, and a torch travel speed of 100 mm/min. The wire was manually fed at approximately 160 mm/min, maintaining a constant 3 mm distance from the tungsten tip to the workpiece. High-purity argon gas (99.99 %) was employed as both the primary and trailing shielding gas at a flow rate of 15 L/min to prevent oxidation. A 30-second interval was maintained between layers for controlled cooling. Prior to each new layer, the deposited surface was mechanically cleaned using a stainless steel brush to remove spatter and surface contaminants.

2.2. Molten salt corrosion testing

Rectangular specimens (12 mm × 10 mm × 1.2 mm) were extracted via wire electrical discharge machining (EDM) from three regions: the WAAM NiMoCr cladding, the 316 L substrate, and a bimetallic interface sample. Single-material samples consisted entirely of either 316 L or NiMoCr cladding. For the bimetallic interface samples, each portion of 316 L and NiMoCr is cut to approximately 12 mm × 10 mm × 0.6 mm. All specimens were polished to remove surface oxidation and expose fresh surfaces prior to corrosion testing.

A vitreous (glassy) carbon crucible (70 mm diameter, 70 mm height, 250 mL capacity) was filled with the homogeneous FLiNaK mix, in a glove box under a nitrogen atmosphere. The vitreous carbon crucible was then lowered into a graphite crucible liner at the base of a furnace, pre-heated to 150 °C. Temperature was gradually raised at a heating rate of 3 °C/min under vacuum to melt the eutectic salt (melting point 454 °C) and to remove residual water and volatile impurities from the molten salt. Total duration of furnace and salt conditioning spanned approximately 48 h. Argon gas (99.997 % pure) was then used to purge the furnace and provide an inert testing environment.

To simulate localized cladding failure that may expose the underlying steel during long-term service, the NiMoCr cladding and 316 L substrate were corroded together in the same molten-salt environment. This configuration reproduces the coupled corrosion behavior expected under such worst-case conditions. Future work will include comparative tests on stand-alone 316 L substrates and NiMoCr claddings to quantitatively evaluate cladding protection efficiency. Each sample was suspended using Ni wires to ensure full immersion in molten FLiNaK and

Table 1
Chemical compositions of the wire and substrate materials (wt%).

Composition	Ni	Mo	Cr	Fe	Mn	Al	Si	C	P	S
Wire (NiMoCr)	Bal.	16.40	6.89	3.62	0.58	0.06	0.43	0.05	0.002	< 0.001
Substrate (316 L)	10.00–14.00	2.00–3.00	16.00–18.00	Bal.	≤ 2.00	-	≤ 1.00	≤ 0.030	≤ 0.045	≤ 0.030

was electrically connected, while avoiding contact with the crucible walls. Three specimens from each material group were tested at 750 °C for 500 h under an argon atmosphere. After corrosion testing, residual salt was removed by soaking the samples in a 20 wt% $Al(NO_3)_3$ aqueous solution for 24 h. Mass changes were measured before and after exposure using a high-resolution balance, with each value representing the average of three measurements. Sample dimensions were carefully measured before and after corrosion testing. Weight loss and corrosion rate were calculated over the exposed area.

2.3. Microstructure characterisation

Cross-sectional specimens from both as-fabricated and post-corrosion conditions were prepared for electron backscatter diffraction (EBSD) and energy-dispersive X-ray spectroscopy (EDS) analyses. Samples were mounted in conductive resins, mechanically polished using 3 μm and 1 μm diamond suspensions, and finally finished with a 15-nm colloidal silica suspensions. Transmission electron microscopy (TEM) specimens were prepared using a Zeiss Auriga 60 focused ion beam (FIB) system. A protective platinum layer was first deposited before coarse milling, followed by lift-out and thinning to electron transparency.

Microstructural characterization was conducted using a Zeiss® Ultra Plus Scanning Electron Microscope (SEM) equipped with EBSD and EDS detectors. Simultaneous EBSD and EDS mapping was carried out at 20 kV with a step size of 150 nm, an aperture size of 120 μm, stage tilt of 70°, and working distance of 14.5 mm. The SEM images were taken with forescatter detectors associated with the EBSD Symmetry detector. EBSD data were processed using the MTEX toolbox [36]. TEM imaging was performed on a JEM 2200FS operated at 200 kV.

2.4. Thermodynamic simulations

Thermo-Calc software (v2024b) [35] was used to simulate microsegregation and phase evolution during WAAM solidification and subsequent high-temperature corrosion exposure. A Scheil-Gulliver model with solute trapping was employed to simulate the solidification of NiMoCr alloys with varying Fe contents. Solute partitioning between the liquid and solid γ-phase were analyzed to assess element segregation. To quantify element diffusion across dendrites, one-dimensional simulations were conducted using the DICTRA module. The domain size represented half the measured primary dendrite arm spacing (PDAS). Simulations were conducted using the TCN12 thermodynamic and MOBNI6 mobility databases for Ni-based alloys.

To evaluate the influence of chemical elements on the precipitate evolution during high-temperature corrosion, precipitation simulations at 750 °C were performed using the TC-PRISMA module. These simulations modeled the nucleation, growth, and coarsening behavior of precipitates in interdendritic regions over 500 h, assuming grain edges as preferred nucleation sites. In addition, one-axis equilibrium calculations were conducted to assess the effect of Mo content on elemental diffusion coefficients at 750 °C. Further details are provided in conjunction with the interpretation of the corresponding simulation results.

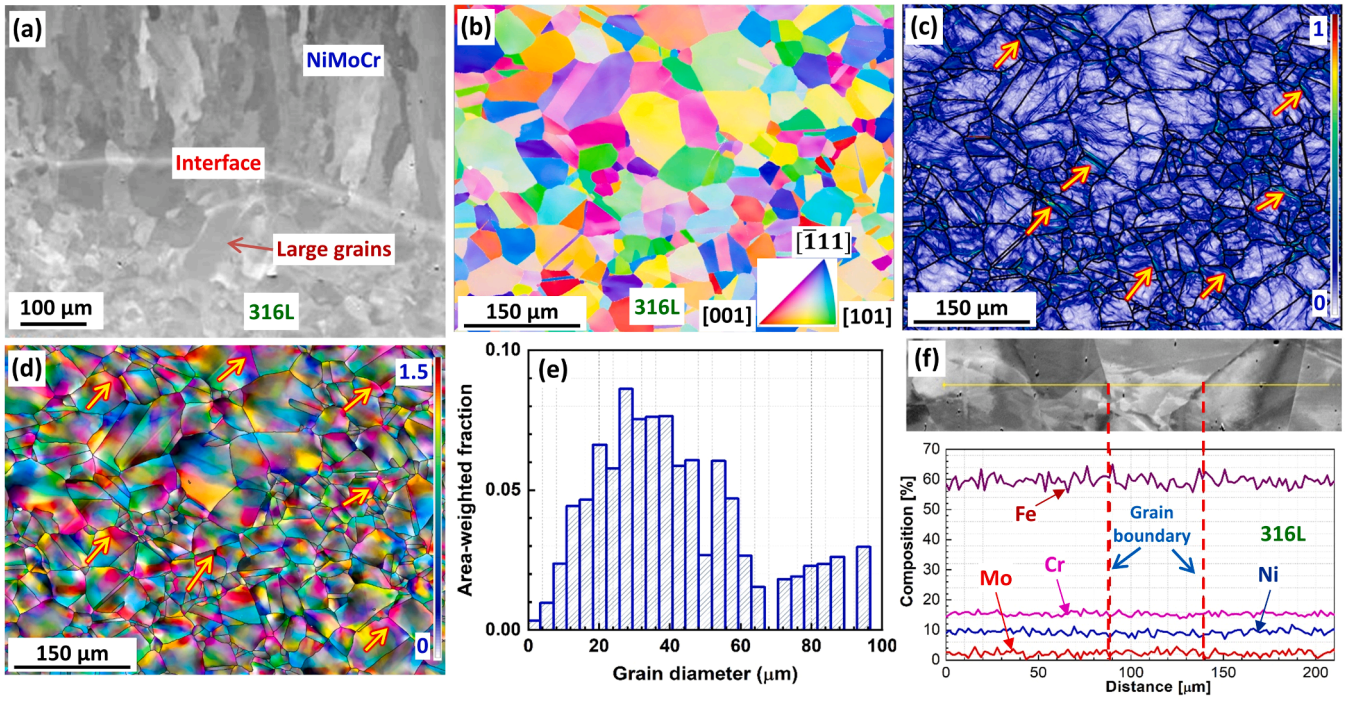


Fig. 1. Cross-sectional overview of the WAAM NiMoCr alloy cladded 316 L bistructure and detailed microstructural characterization of the steel substrate. (a) SEM cross-sectional image of the bistructure, and (b-f) EBSD and EDS analyses of the steel substrate, including: (b) grain orientation map with color coding by crystallographic orientations, (c) misorientation-to-mean map, (d) kernel average misorientation map, (e) grain size distribution, and (f) EDS line scan across representative grains. Arrows in (c) and (d) indicate regions of elevated misorientation near grain boundaries. Legends in (c) and (d) show misorientation-to-mean and KAM values in degrees, respectively.

3. Results

3.1. As-fabricated microstructure

Fig. 1 shows a cross-sectional overview of the WAAM NiMoCr clad-ded 316 L bistructure, along with detailed microstructural character-ization of the steel substrate. The SEM image of the bistructure cross-section (Fig. 1a) reveals epitaxal growth of elongated columnar grains in the NiMoCr cladding, while the 316 L substrate maintains an equiaxed grain structure (Figs. 1a and 1b). Notably, large grains are observed in the substrate near the cladding-substrate interface, with some extending across the interface into the cladding, a feature which will be discussed in detail later. EBSD misorientation-to-mean and kernel average misorientation (KAM) maps (Figs. 1c and 1d) of the steel substrate reveal intragranual substructures. The misorientation-to-mean parameter rep-resents the angular deviation of a point relative to the grain's average orientation, whereas KAM quantifies the local misorientation with respect to neighboring points. Higher values of both parameters, particularly near grain boundaries (indicated by arrows in Figs. 1c and 1d), suggest enhanced stored energy and dislocation density in these regions, indicating the presence of significant lattice defects. The grain diameter distribution is shown in Fig. 1e, revealing that most grains fall within the range of 15–60 μm, with an average grain diameter of approximately 19 μm. Nevertheless, the EDS line scan (Fig. 1f) shows no significant segregation of Ni, Mo, Cr, or Fe near the grain boundaries within the substrate.

Further microstructural characterization of the NiMoCr cladding is present in Fig. 2. High-magnification SEM image (Fig. 2a) reveals bright precipitates embedded within the columnar grain matrix, consistent with previous reports on WAAM Ni-based alloys [5–7]. EBSD orientation mapping (Fig. 2b) shows typical $< 001 >$-oriented grains closely aligned with the build direction, confirming preferentially growth of γ-matrix grains along the $< 001 >$ orientation, as observed in the WAAM Hastelloy C276 Ni alloy [24]. The misorientation-to-mean map (Fig. 2c) exhibits intragranular dendritic substructures characterized by orientation gradients. These appear as subgrains with low-angle boundaries (1°–10° misorientation) embedded within large columnar grains (misorientation ≥10°), resulting from accumulated orientation differences across dendritic arms. EDS elemental maps (Fig. 2d) and line scan (Fig. 2e) illustrate severe Mo enrichment and Ni depletion in interdendritic regions, accompanied by moderate Fe depletion and slight Cr enrichment. A representative interdendritic precipitate exhibits ~34 wt% Mo and ~42 wt% Ni. Given the 0.05 wt% carbon content in the feedstock, these are likely Mo-rich carbides, which will be further assessed in the Discussion section. These results indicate that the WAAM process produces a highly textured columnar dendritic microstructure

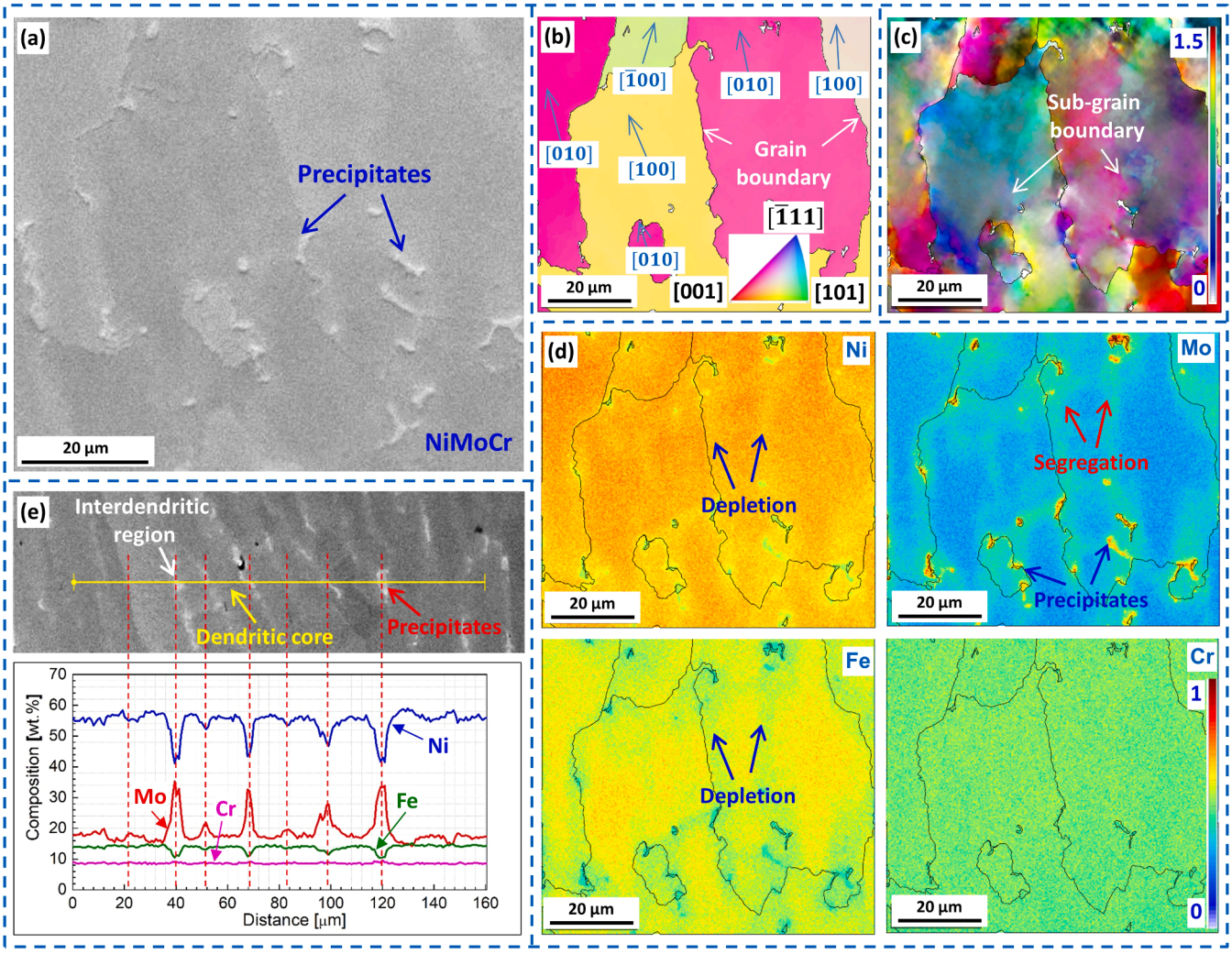


Fig. 2. Microstructural characterization of the NiMoCr cladding. (a) SEM morphology, (b) EBSD grain orientation map, (c) EBSD misorientation-to-mean map, (d) EDS elemental maps of Ni, Mo, Fe, and Cr, and (e) EDS line scan across dendrites. The color key in (b) represents distinct grain orientations, while the legends in (c) and (d) indicate misorientation-to-mean values and element distribution levels, respectively.

with distinct subgrains, significant Mo segregation and minor carbide formation in the interdendritic regions, in contrast to the equiaxed microstructure typically observed in wrought Ni-based alloys [6].

The composition transition region between the NiMoCr cladding and the 316 L substrate exhibits a graded microstructure and composition (Fig. 3). Fig. 3a shows a high-magnification view of the interface region, where the dendritic features and Mo-enriched interdendritic precipitates of the NiMoCr cladding are more clearly revealed compared with the low-magnification overview in Fig. 1a. The SEM image with atomic contrast (Fig. 3a) reveals a gradual contrast shift from Fe-rich to Ni-rich regions. EBSD maps (Figs. 3b and 3c) show continuous grain elongation across the interface, with no distinct microstructural boundary, suggesting epitaxial growth. This differs from our previous report, where a distinct boundary formed between WAAM C276 cladding and P91 steel substrate [24]. EDS maps (Fig. 3d) and line scan (Fig. 3e) reveal a transition zone of approximately 81 μm wide, characterized by increasing Ni and Mo and decreasing Fe and Cr from the substrate toward the cladding across individual grains, forming what we define as compositionally graded grains (CGGs).

TEM analyses (Fig. 4) provide further evidence of the CGGs. The TEM micrograph (Fig. 4b) reveals a triple junction of grain boundaries and a high density of dislocations within the matrix, attributed to thermally induced plastic deformation caused by repeated heating and cooling cycles during deposition [37]. Compositional profiling across the cladding-substrate interface (Fig. 4c) confirms smooth variations in Ni, Mo, Fe and Cr contents. Selected area diffraction (SAD) patterns (Fig. 4a) taken along the [110] zone axis confirm a single FCC γ-phase (*Fm*$\bar{3}$*m*, space group *No. 225*) across the transition. Measured lattice parameters vary with composition: ~3.55 Å at 57 wt% Fe / 22 wt% Ni, ~3.48 Å at 42 wt% Fe / 36 wt% Ni, and ~3.49 Å at 28 wt% Fe / 45 wt% Ni, indicating lattice contraction with Ni enrichment. This is consistent with reported Fe–Ni alloy behavior, where the lattice constant increases with the Ni content up to ~35 wt% and then decreases with further Ni addition [38]. These findings confirm the presence of CGGs with smooth compositional and crystallographic continuity across the cladding-substrate interface.

3.2. Molten salt corrosion performance

Fig. 5 presents corrosion performance of samples tested in this study,

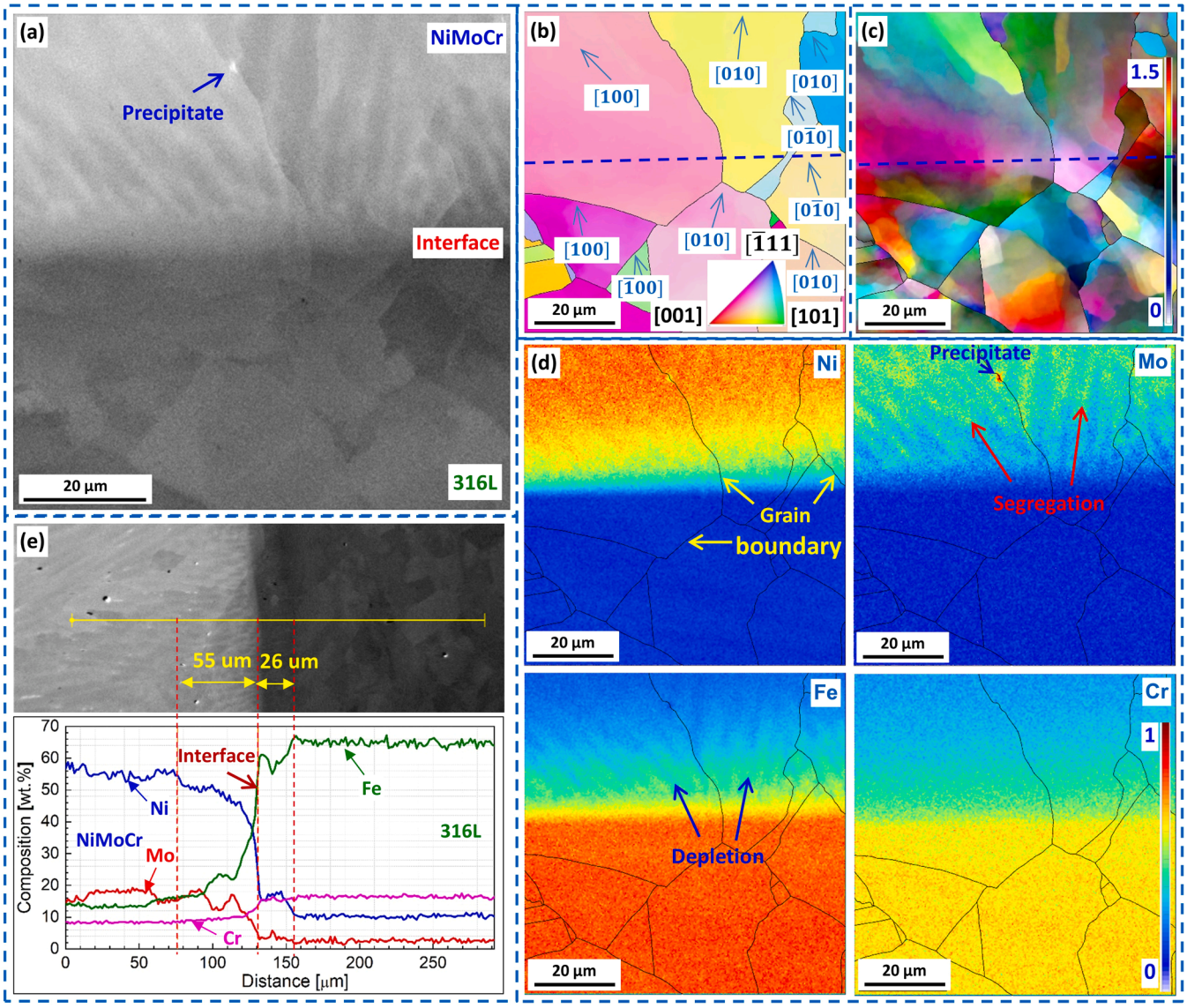


Fig. 3. Microstructural characterization of the transition region between the NiMoCr cladding and the 316 L substrate. (a) SEM morphology, (b) EBSD grain orientation map, (c) EBSD misorientation-to-mean map, (d) EDS elemental maps of Ni, Mo, Fe, and Cr, and (e) EDS line scan across the transition region. The color key in (b) represents distinct grain orientations, while the legends in (c) and (d) indicate misorientation-to-mean values and element distribution levels, respectively.

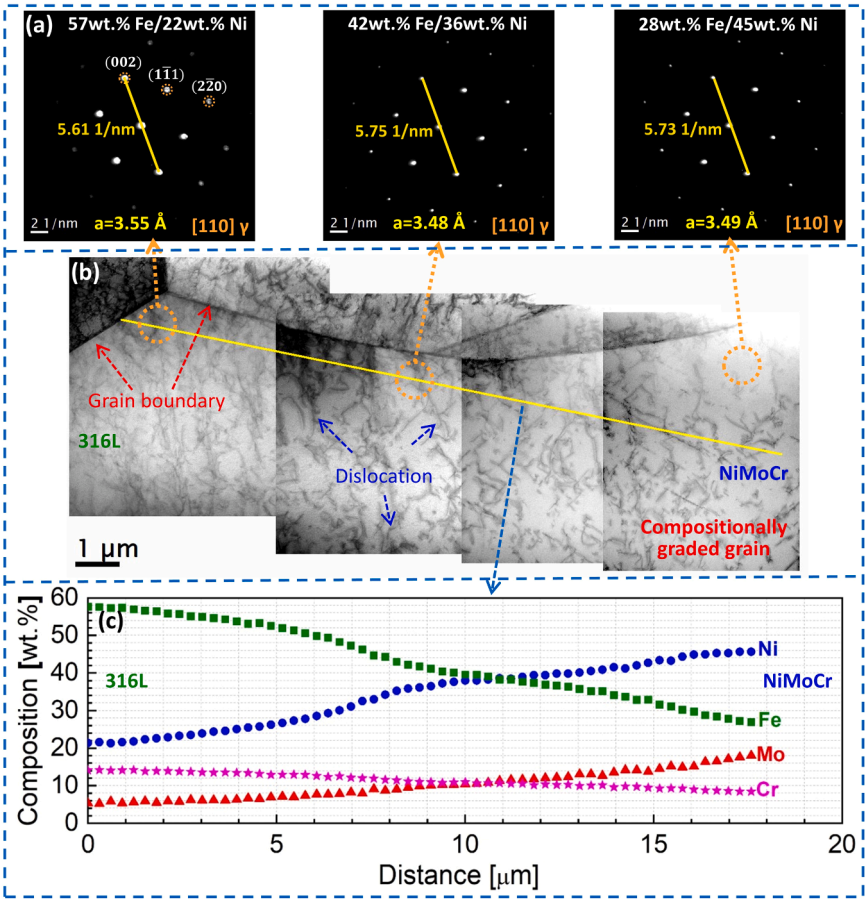


Fig. 4. TEM micrographs illustrating chemical composition and lattice parameter variations across the transition region in WAAM NiMoCr alloy cladded 316 L stainless steel. (a) SAD patterns from regions with different compositions, (b) TEM micrograph highlighting the line scan region used for composition analysis, and (c) elemental composition profile across the transition from the 316 L steel substrate to the NiMoCr alloy cladding.

along with a comparison with previously reported data. The corrosion rate, $\dot{c}$, was calculated using the following equation [14]:

$$\dot{c} = \frac{87.6\ W}{\rho_m A t} \tag{1}$$

where W is the weight loss (mg), $\rho_m$is the specimen density (g/cm^3), A is the exposed surface area (cm^2), and t is the exposure time (h). The constant 87.6 accounts for unit conversions to express corrosion rate in mm/year.

As shown in Fig. 5a, the WAAM NiMoCr cladding exhibits the highest corrosion resistance among the three sample types, with the lowest average weight loss (5.67 mg/cm^2) and corrosion rate (0.11 mm/year). In contrast, the 316 L substrate shows significantly higher degradation, with an average weight loss of 12.92 mg/cm^2 and a corrosion rate of 0.29 mm/year. The bistructure samples, containing both cladding and substrate regions, exhibit intermediate values, with an average weight loss of 8.57 mg/cm^2 and a corrosion rate of 0.18 mm/year. The small error across replicates indicate good reproducibility and suggest uniform microstructures and compositions within each sample group. These results demonstrate the excellent corrosion resistance of the WAAM NiMoCr cladding, which effectively shields the underlying steel from severe degradation in high-temperature molten fluoride salt environments. The intermediate corrosion performance observed in the bistructure further supports the protective role of the cladding and underscores a graded corrosion response governed by the microstructure and chemical gradients in the transition zone.

Fig. 5b compares the corrosion rates obtained in this study with those reported for conventionally fabricated NiMoCr alloys [4,6,7,10,31,39–49] and 316 stainless steels [10,30,32,43,44,50–53] in molten fluoride salts. While most prior studies were conducted at 700 °C, relatively few data are available at 750 °C or higher. Although corrosion rate typically increases with temperature, some reported corrosion rates at 750 °C or 850 °C are lower than those at 700 °C and below. This discrepancy highlights the sensitivity of corrosion behavior to experimental conditions, including salt purity (e.g., oxygen [40], moisture [4], CrF_3 [10], and graphie particles [41,51]), applied stress [31], materials processing history [46], and containment materials such as crucibles [53] or capsules [30]. The corrosion rates measured in this study are slightly higher than those reported for trandtionally fabricated GH3535 alloy under the same corrosion temperature and durtion. One possible explanation is galvanic interaction between the NiMoCr clading and the 316 L substrate, which may accelerate the degradation of the steel substrate [32]. This mechanism is further discussed in the Discussion section.

3.3. Post-corrosion microstructural evolution

Microstructural characterization of the corroded samples was performed to elucidate the degradation mechanisms induced by molten salt exposure. Fig. 6 presents the surface morphology and cross-sectional SEM images, highlighting the distinct corrosion responses of the NiMoCr cladding and the 316 L substrate. On the molten-salt-exposed surface, pronounced grain boundary grooves are observed in the 316 L substrate (Fig. 6a), whereas the NiMoCr cladding exhibits a comparatively flat and less corroded surface (Fig. 6b). In the cross-section views, residual corrosion-affected layers are observed on both the NiMoCr alloy

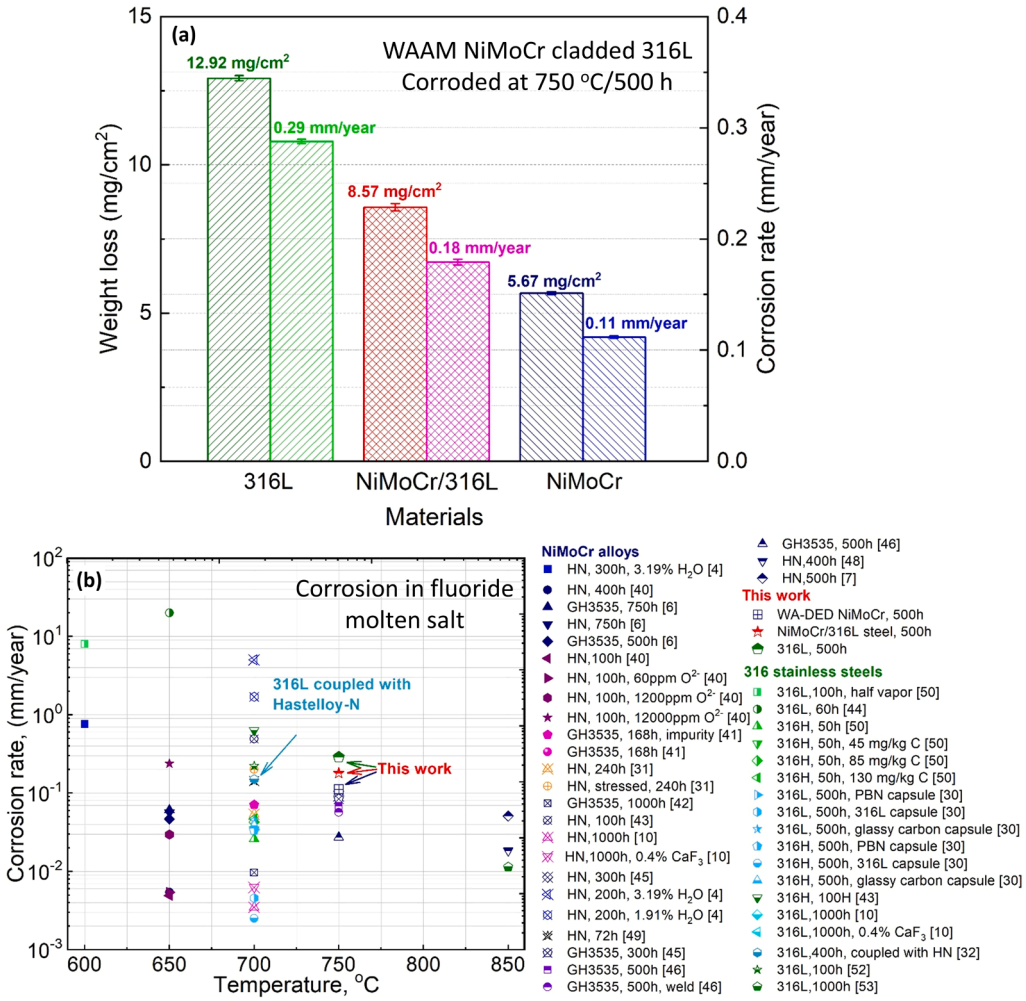


Fig. 5. Corrosion performance of samples in this study and comparison with reported data. (a) Weight loss and calculated corrosion rates for samples extracted from the 316 L substrate, bistructure, and NiMoCr cladding after exposure to molten FLiNaK salt at 750 °C for 500 h, and (b) comparison of corrosion rates from this study with previously reported values for NiMoCr alloys and 316 stainless steels fabricated by conventional methods in molten fluoride salts.

and steel sides (Figs. 6c and 6d). However, the 316 L substrate exhibits significantly more severe corrosion damage than the NiMoCr cladding (Fig. 6d), consistent with the greater weight loss measured for the steel substrate. The high-magnification SEM image of the steel side (Fig. 6e) reveals deep, elongated grooves along grain boundaries within the residual corrosion-affected layer, indicative of pronounced intergranular corrosion. In contrast, the WAAM NiMoCr cladding displays a markedly different corrosion morphology (Figs. 6f and 6g). The corroded surface is uneven, with grooves concentrated in dendritic cores and raised bulges in interdendritic regions. This morphology reflects intradendritic corrosion, which contrasts with the intergranular attack typically observed in conventionally fabricated NiMoCr alloys under similar conditions [28]. Notably, more than 70 % of corrosion bulges occur near Mo-enriched interdendritic zones, indicating a strong correlation between localized corrosion and compositional heterogeneity. Precipitates frequently appear near the leading edges of these bulges, suggesting that they may impede local corrosion propagation and contribute to the corrosion resistance of the WAAM cladding. Thickness measurements of the residual corrosion-affected layers further support this disparity in corrosion resistance. The steel substrate retains a significantly thicker residual corrosion-affected layer (~71 μm, Fig. 6e), whereas the NiMoCr cladding exhibits only a ~6 μm layer (Fig. 6g), underscoring the superior performance of the WAAM NiMoCr alloy in high-temperature molten salt environments.

To further examine the corrosion-induced microstructural changes, SEM-EDS and TEM analyses were performed. Fig. 7 shows EDS elemental maps and line scans from representative regions of the steel substrate. Substantial enrichment of Cr and O on the residual corrosion-affected layer (Fig. 7a, Cr and O maps) is observed, confirming the formation of Cr-rich corrosion products. In contrast, Fe, Cr, and Ni concentrations are markedly reduced within the grain boundary grooves, suggesting near-complete dissolution of material along grain boundaries into the molten salt. Additionally, Cr depletion extends beyond the grooves along grain boundaries, forming a continuous, interconnected depletion network within the residual corrosion-affected layer. Notably, such depletion is not observed for Fe or Ni; instead, Fe and Ni segregation are evident within grooves. EDS line scans reveal a Cr-depleted zone of approximately 5.3 μm thick within the exposed grain matrix (Fig. 7b), while a broader depletion zone (~13.7 μm) is observed along grain boundaries (Fig. 7c). Cr depletion extends deeper into the matrix along the grain boundary, tapering in width (Fig. 7a, Cr map), suggesting that Cr depletion precedes and facilitates localized corrosion along grain boundaries. These findings indicate that the intergranular corrosion observed in the steel substrate is driven by selective Cr depletion and subsequent dissolution of alloy constituents.

A site-specific TEM lamella was extracted across a corroded grain boundary containing corrosion products and precipitates using FIB milling (Fig. 8a). Two major phases are identified in the SEM image (Fig. 8a): a dominant gray phase and a minor white phase, corresponding to contrasting features in the bright-field TEM image (Fig. 8b).

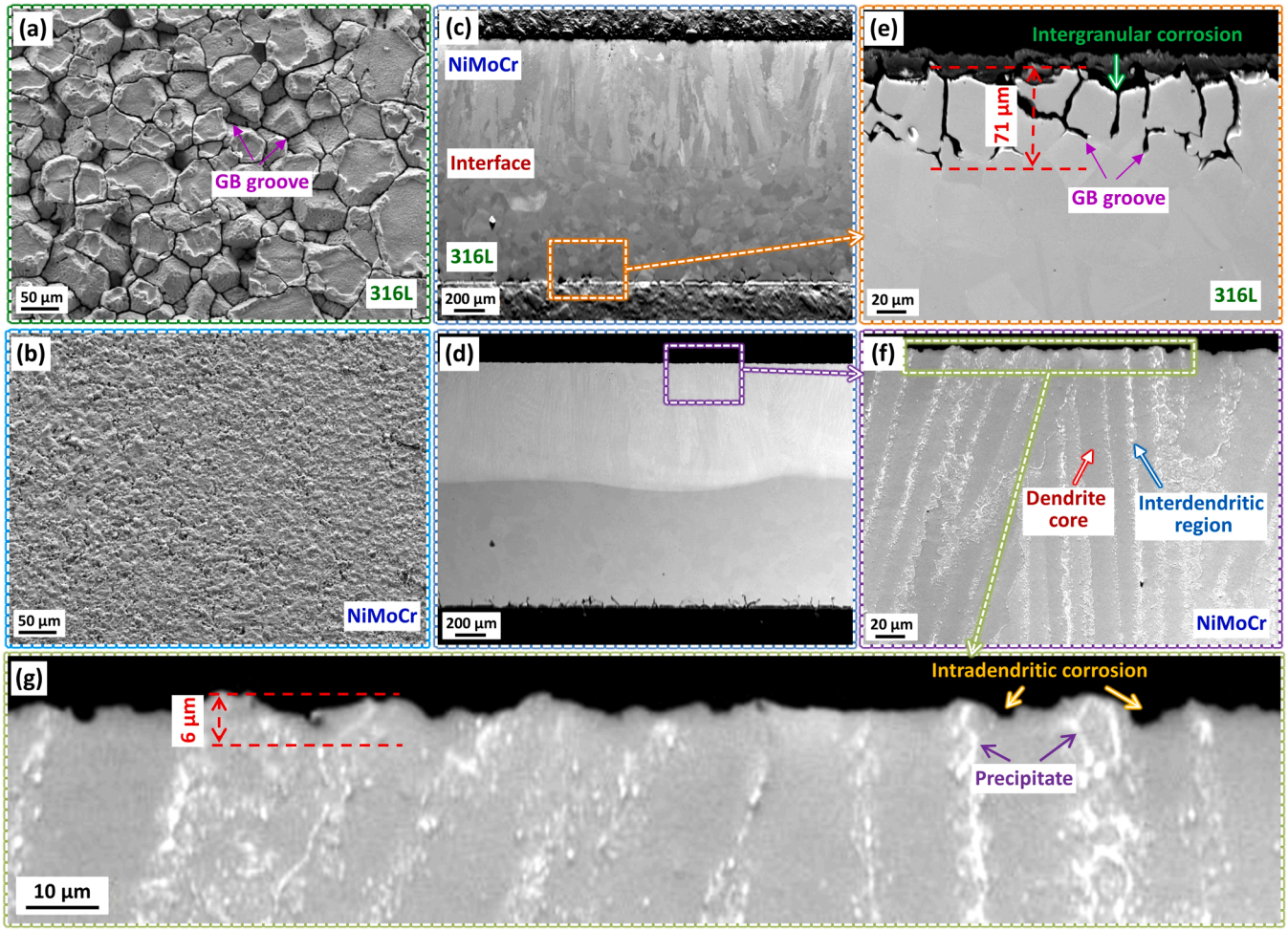


Fig. 6. SEM micrographs showing the surface morphology and cross-sectional microstructure of post-corrosion samples. Surface morphology: (a) 316 L substrate and (b) NiMoCr cladding. Cross-section microstructure: (c) Orientation contrast SEM image of the NiMoCr/316 L bistructure, (d) atomic number contrast SEM image of the same region, (e) SEM image of the 316 L substrate side, (f) SEM image of the NiMoCr cladding side, and (g) high-magnification SEM image of the boxed area in (d).

SAD patterns from the gray phase are indexed to Cr_2O_3 (space group $R\bar{3}c$, ICSD 167368) along the [012] zone axis. The corresponding EDS spectrum (Fig. 8c) confirms the presence of Cr and O, with some Cu signal attributed to the supporting grid. Quantitative EDS analysis yields an average composition of ~61.81 wt% Cr and 38.17 wt% O, further confirming Cr_2O_3 as the dominant corrosion product. The dark-contrast phase observed in TEM is enriched in Mo and Fe (Fig. 8d), and SAD patterns are consistent with the μ phase (space group $R\bar{3}mH$, ICSD 632622) viewed along the [153] zone axis. The Mo-enriched μ phase has been reported to form intrinsically within 316 stainless steel during prolonged thermal exposure at elevated temperatures, even in the absence of molten salt [54]. Therefore, in this study, the observed μ phase in the interior of the 316 L substrate is more reasonably attributed to thermal exposure rather than a direct corrosion product. Meanwhile, Cr depletion from the steel substrate likely facilitated the formation of Cr_2O_3 through reactions with oxygen-containing impurities in the molten salt.

Fig. 9 presents EDS elemental maps and line scans from representative regions of the corroded WAAM NiMoCr alloy cladding. A markedly higher density of Mo-enriched precipitates is observed in the interdendritic regions compared to the as-fabricated condition (Fig. 2), indicating that dynamic precipitation occurred during exposure to molten salt at 750 °C for 500 h. Quantitative image analysis revealed that the area fraction of Mo-enriched precipitates in the interdendritic regions increased from approximately 1.1 % in the as-fabricated cladding (Figs. 2a) to 11.5 % after corrosion (Fig. 9a), indicating an order-of-magnitude increase in precipitate density. These precipitates are predominantly located at the leading edges of the corrosion bulges (Fig. 9a, Mo map), suggesting their strong resistance to corrosion attack. A shallow corrosion front is evident, characterized by Cr depletion, as revealed by the EDS line profiles. The extent of Cr depletion varies with microstructural location, reaching approximately 5.6 μm in the dendritic core (Figs. 9b) and 10.2 μm in the interdendritic region (Fig. 9c). It is worth noting that the Cr content in the interdendritic region is affected by the presence of Cr-depleted precipitates, which may influence the apparent depletion depth. Notably, the interdendritic regions show relatively improved corrosion resistance compared to the dendritic cores.

Fig. 10 shows TEM characterization of the dynamically formed precipitates within the corroded NiMoCr alloy cladding. Dense populations of irregular, blocky precipitates are found predominantly in the interdendritic regions (Fig. 10a). The larger precipitates exhibit an average composition of approximately 71.22 wt% Mo and 19.85 wt% Ni (Fig. 10b). SAD patterns acquired from one precipitate (Fig. 10d) are indexed to the topologically close-packed (TCP) σ phase (space group $P4_2/mnm$, ICSD 188709), viewed along the [145] zone axis. The σ phase, along with other TCP phases such as μ, *P*, and *R*, are known to form in Ni-based alloys during high-temperature exposure or prolonged service [24,55,56]. There is no evidence that corrosion promoted the formation of the σ phase. In addition to the σ phase, a minority population of

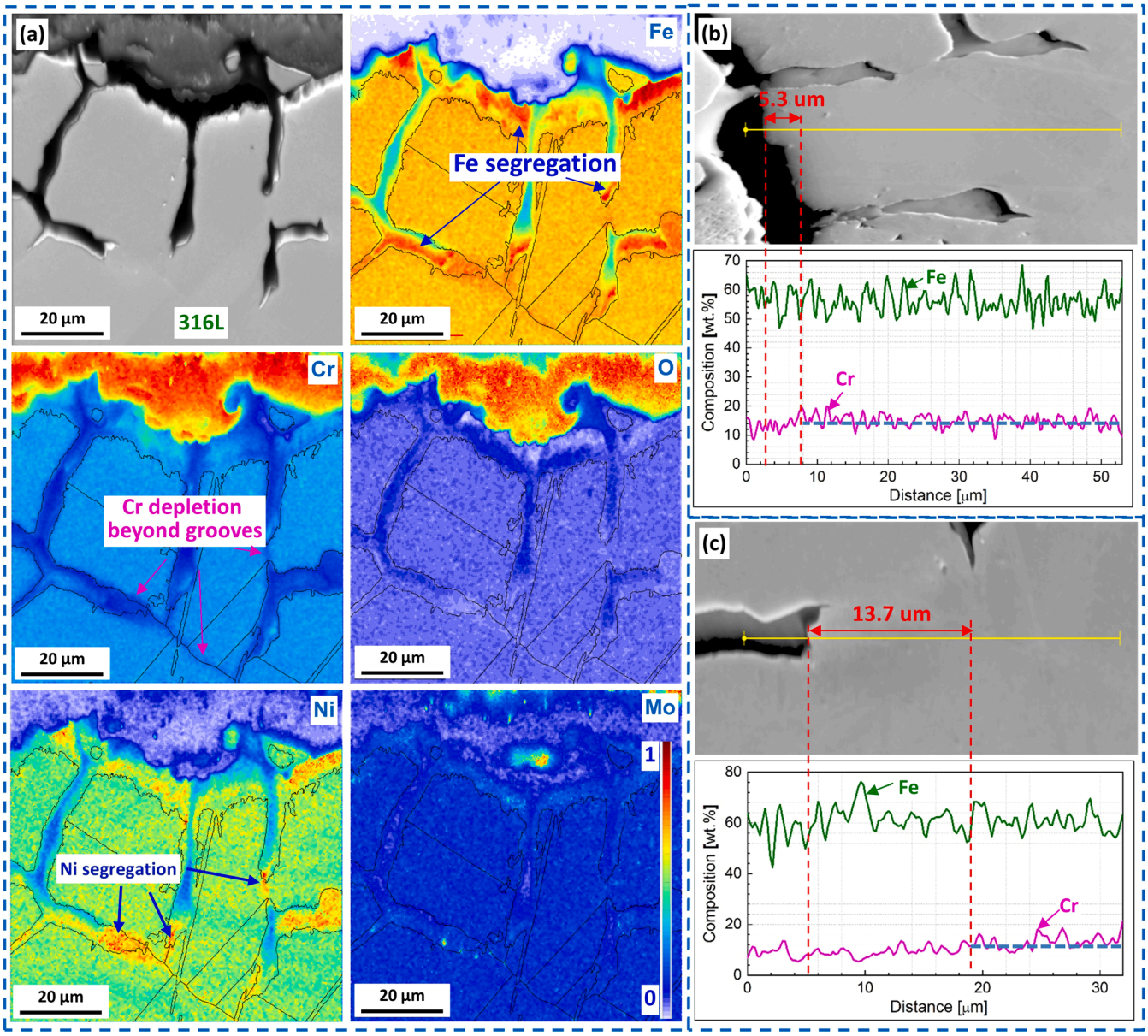


Fig. 7. Post-corrosion microstructural and compositional analyses of the 316 L steel substrate. (a) SEM image and corresponding EDS elemental maps of Fe, Cr, O, Ni, and Mo, with an inset color legend in the Mo map indicating element levels, (b) EDS line scan across a grain interior, and (c) EDS line scan along a grain boundary.

quadrilateral precipitates was identified. These precipitates exhibit a similar Mo-Ni-rich composition (~64.83 wt% Mo, ~22.53 wt% Ni). The corresponding SAD patterns (Fig. 10e) are consistent with a Mo-rich carbide phase, most likely M_6C (space group $Fd\bar{3}m$, ICSD 76134), viewed along the [120] zone axis, although the possible presence of other Mo-rich carbides (e.g., $M_{12}C$) cannot be fully ruled out. These carbides, present in limited amounts, may have formed during the WAAM process, as similar features were observed in the as-deposited condition (Fig. 2). Overall, these results indicate that corrosion at 750 °C promotes the precipitation of Mo-rich TCP phases, primarily σ, in the interdendritic regions of the WAAM NiMoCr alloy cladding.

Fig. 11 presents EDS maps and line scans across the corroded NiMoCr/316 L bistructure, revealing compositional and microstructural evolution across the cladding-substrate interface. The EDS maps in Fig. 11a and corresponding line scan in Fig. 11b delineate the NiMoCr alloy cladding, a compositionally graded region, and the underlying 316 L steel substrate. CGGs are clearly visible within the transition zone (Figs. 11a and 11b), and the density of dynamically formed Mo-rich precipitates increases progressively from the cladding-substrate interface toward the NiMoCr cladding (Fig. 11a, Mo map). The corrosion product Cr_2O_3 is primarily distributed along the steel substrate side (Fig. 11a, Cr map and O map), consistent with earlier observations. A pronounced grain boundary corrosion groove originating from the steel substrate extends across the interface but terminates at the interdendritic precipitate network on the NiMoCr alloy side (Fig. 11a). Notably, the transition region exhibits markedly reduced corrosion damage compared with the steel, effectively serving as a corrosion buffer between the susceptible steel and the more corrosion-resistant NiMoCr alloy. These results indicate that the CGGs produced in this FCC-to-FCC system provides an intermaterial interface that is not preferentially attacked in the WAAM NiMoCr alloy cladded steel bistructure under high-temperature fluoride molten salt environments.

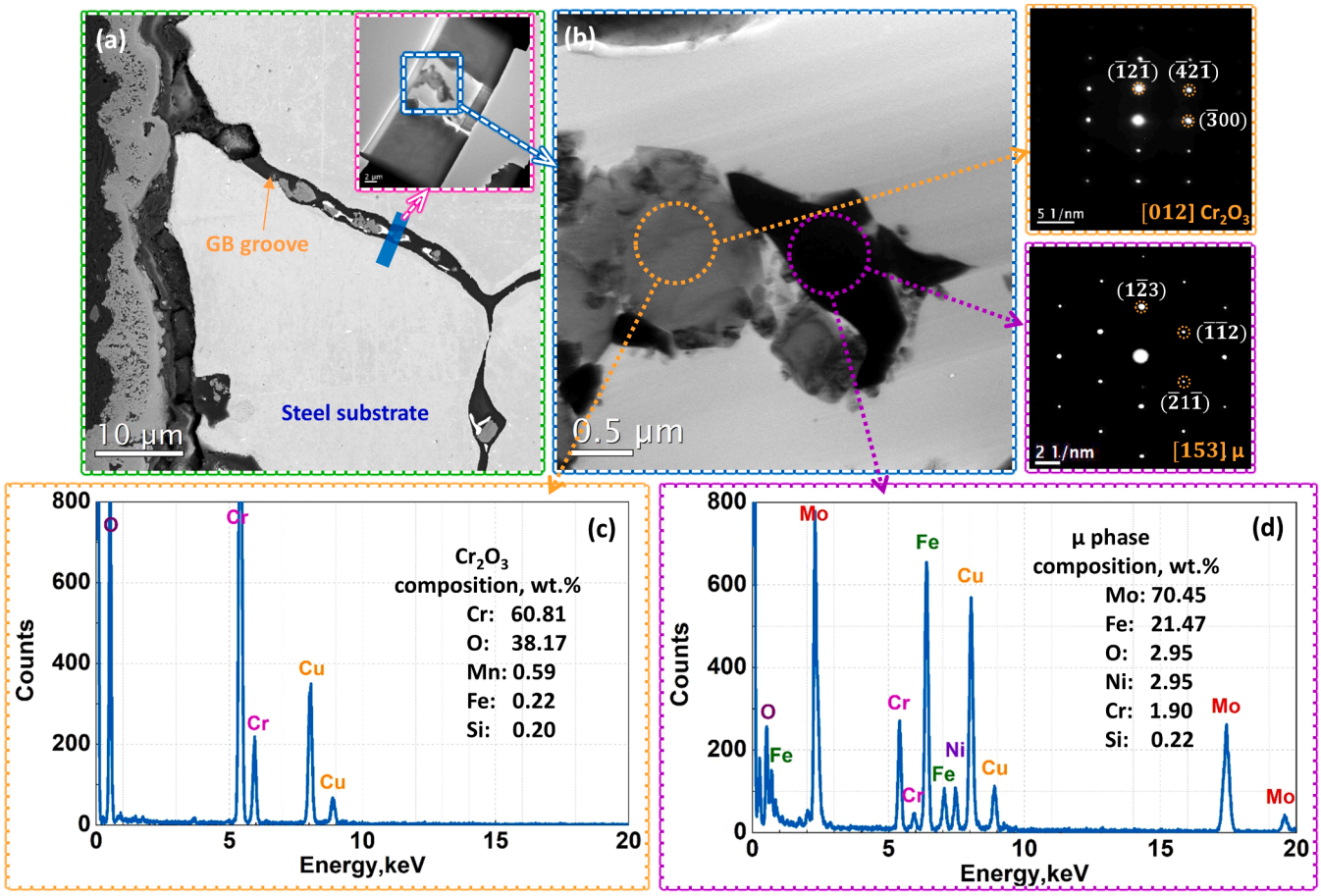


Fig. 8. SEM and TEM micrographs with chemical composition analyses of corrosion products and second-phase particles in a grain boundary groove of a post-corrosion 316 L sample. (a) SEM image showing the grain boundary groove, with an inset SEM image indicating the TEM specimen location, (b) TEM morphology and corresponding SAD patterns of the corrosion products and precipitates, and EDS spectra and average composition of (c) the corrosion products and (d) the precipitates.

4. Discussion

4.1. Development of complex microstructure features in WAAM NiMoCr alloy cladded 316 L stainless steel

The WAAM process involves localized melting of the wire feed and underlying steel substrate or previously deposited layers using a gas tungsten arc welding torch. This forms a molten pool that solidifies rapidly as the torch traverses the substrate or existing layers [24]. Due to the small volume of molten metal and rapid dissipation of heat, the cooling rates are relatively high [24,57,58]. Concurrently, the surrounding solid material absorbs thermal energy, resulting in localized temperature increases. The extent of this thermal effect diminishes with distance from the molten pool, giving rise to a heat-affected zone (HAZ). Multiple passes during WAAM expose the material to repeated heating and cooling cycles, effectively subjecting it to cyclic heat treatments [24, 57].

4.1.1. Formation of hierarchical grain structures in the WAAM NiMoCr alloy cladding

Solidification during WAAM is predominantly governed by the thermal gradient, which is typically oriented perpendicular to the solid-liquid interface. This promotes the growth of columnar grains aligned parallel to the build direction [10,12], resulting in the formation of elongated grains with a characteristic dendritic morphology (Fig. 1a). Given the anisotropic interfacial energy of the FCC γ-phase matrix, dendrites preferentially grow along the $< 001 >$ crystallographic orientations [24,57], which aligns with the heat flow direction. This leads to the formation of strongly textured dendritic grains with $< 001 >$ orientation along the deposition direction (Figs. 2 and 3).

During solidification, various phases form depending on the local alloy composition, particularly the Fe content, which is higher in early deposited layers and gradually decreases with increasing build height. Solidification behavior was predicted using Scheil simulations with solute tracking for alloys with varying Fe content (Fig. 12a). The results show that solidification begins with the formation of the γ phase, followed by M_6C carbides as the major secondary phase. Only minor amounts of TCP phases, such as *P* and σ, are predicted at the final solidification stage in alloys with 15–30 wt% Fe (Fig. 12a, inset), suggesting M_6C carbides are the dominant precipitates in the as-deposited microstructure (Fig. 2).

During rapid solidification in WAAM, different elements exhibit distinct segregation behaviors, which are governed by the effective partitioning coefficients (ratio of solute concentration in the solid to the liquid). Coefficients > 1 indicate enrichment in the dendritic core, while values < 1 indicate segregation to interdendritic regions. At a solid fraction of 0.8, the predicted partitioning coefficients are 1.06 for Ni, 1.10 for Fe, ~1.00 for Cr, and 0.80 for Mo (Fig. 12b). These predictions are consistent with experimental observations (Fig. 2), where Mo enrichment and Ni/Fe depletion are evident in the interdendritic regions, while Cr is uniformly distributed.

To further evaluate microsegregation across dendrites, one-dimensional diffusion simulation was conducted using the DICTRA module of Thermo-Calc software. The simulation domain corresponded

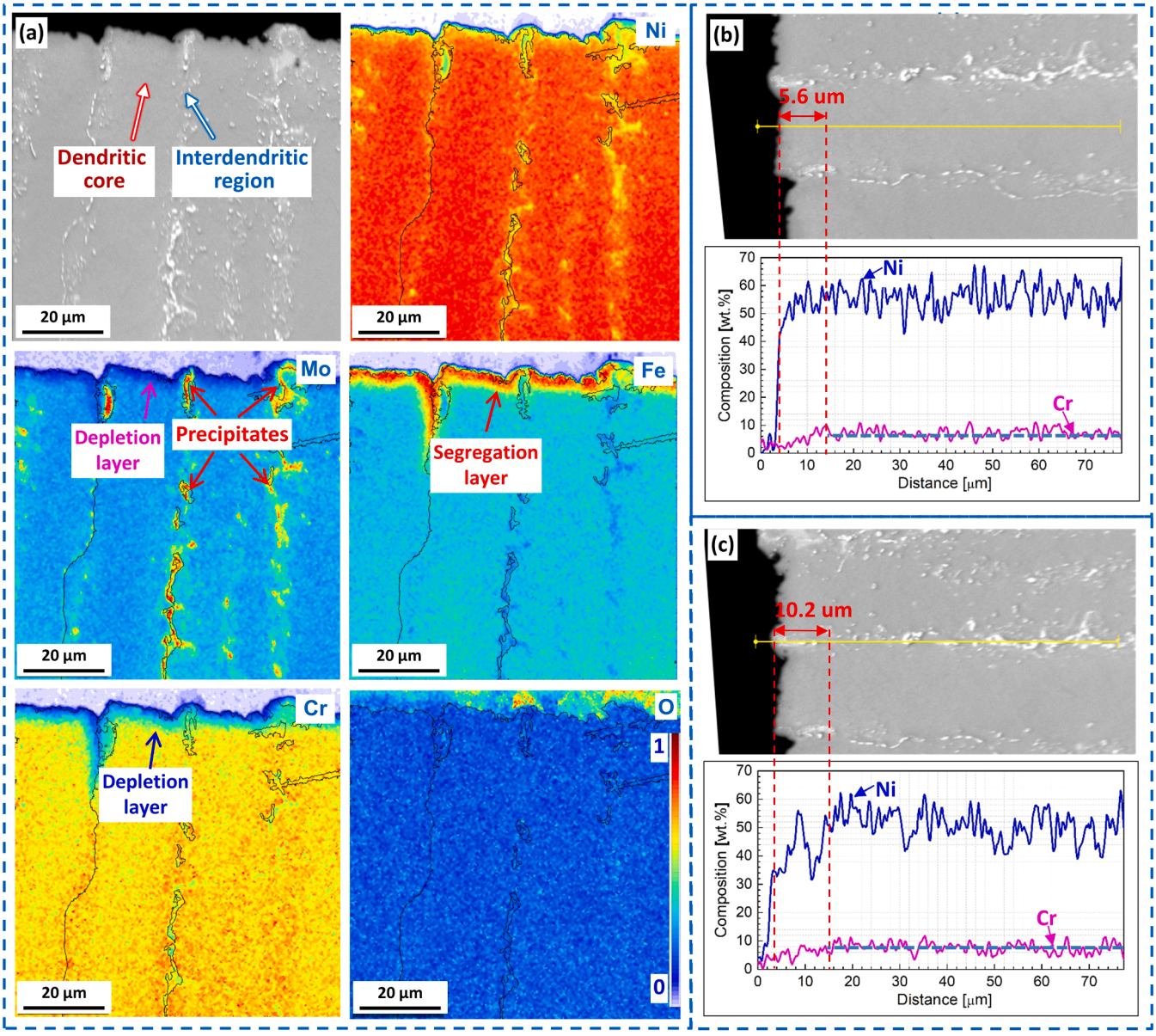


Fig. 9. Post-corrosion microstructural and compositional analyses of the NiMoCr alloy cladding. (a) SEM image and corresponding EDS elemental maps of Ni, Mo, Fe, Cr, and O, with an inset color legend in the O map indicating element levels, (b) EDS line scan across a dendritic core, and (c) EDS line scan across an interdendritic region.

to half of the experimentally measured PDAS, i.e. 8.08 μm, representing the region spanning 51.59–59.65 μm in Fig. 2e. As shown in Fig. 12c, the results confirm significant Mo segregation, minor Cr segregation, and noticeable Fe depletion in the interdendritic region (dendritic boundary in Fig. 12c).

Thus, WAAM NiMoCr alloy cladded 316 L stainless steel exhibits complex hierarchical grain structures composed of columnar dendritic grains, severe Mo segregation and minor carbide formation in interdendritic regions. These features arise from the directional solidification and rapid cooling conditions inherent to WAAM processing.

4.1.2. Formation of compositionally graded grains in the transition region

During WAAM deposition, the molten pool consists of the incoming NiMoCr alloy and a remelted portion of the 316 L substrate. Rapid solidification and limited diffusion restrict extensive mixing, resulting in a Fe-rich zone near the fusion boundary that gradually transitions toward the NiMoCr alloy composition with increasing distance from the substrate.

The formation of compositionally graded grains in this transition region is primarily controlled by two factors. First, the thermal gradient and cooling dynamics dictate the solidification behavior. Under the WAAM conditions used here, the cooling rate decreases progressively from the remelted steel substrate toward the center of the molten pool. This spatial gradient in cooling rate enables grains to grow continuously across the transition region, rather than forming a sharp microstructural boundary. Thermo-Calc–assisted estimates of thermal properties support this behavior, showing that the 316 L substrate provides a moderate cooling rate that does not strongly restrict grain growth at the interface.

Second, the crystallographic compatibility between the cladding and substrate plays a critical role. Both 316 L and the NiMoCr alloy exhibit FCC γ-matrices with similar lattice parameters (~3.55 Å for γ-Fe and ~3.49 Å for γ-Ni). This structural similarity allows epitaxial growth during solidification, enabling grains to extend smoothly from the remelted steel into the Ni alloy with only minor lattice adjustments as the composition evolves.

Together, these thermal and crystallographic factors promote a

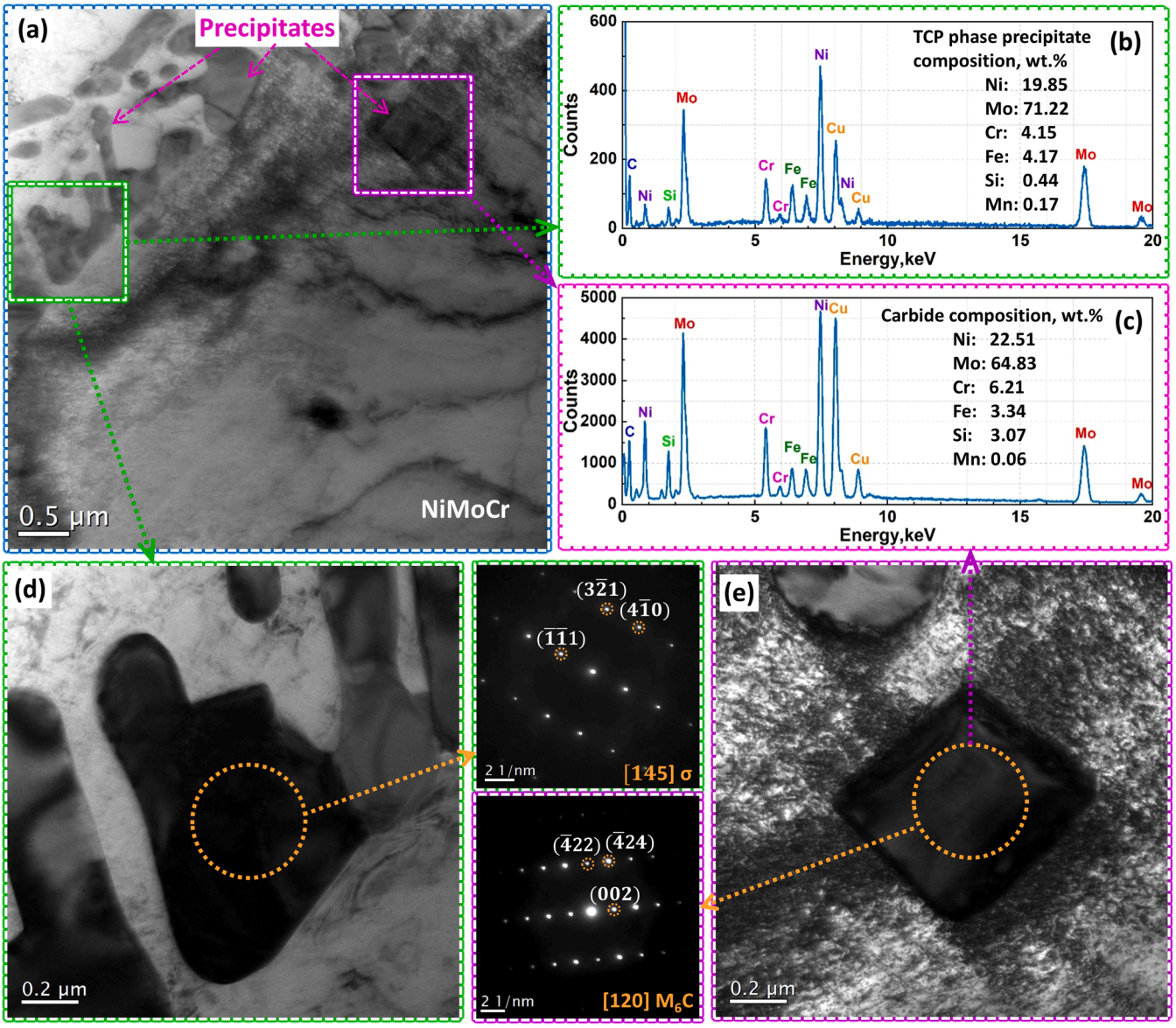


Fig. 10. TEM micrographs and chemical composition analyses of precipitates in the post-corrosion NiMoCr alloy cladding. (a) TEM morphology, (b) EDS spectrum and average composition of TCP phase precipitates, (c) EDS spectrum and average composition of carbides, (d) a TCP phase with corresponding SAD patterns, and (e) a carbide with corresponding SAD patterns.

continuous chemical and microstructural transition across the fusion boundary, giving rise to CGGs in the NiMoCr/316 L system.

4.2. Molten-salt corrosion behavior of WAAM NiMoCr alloy-cladded 316 L stainless steel

In pure fluoride molten salt, metallic materials comtaining key alloying elements such as Ni, Fe, Mo, and Cr generally exhibit resistance to corrosion, as their fluoride formation free energies are less negative than those of the salt constituents [27,59]. However, the presence of impurities, particularly moisture (H_2O), can significantly alter this corrosion resistance [9,27,60]. Corrosion occurs chemically via oxidation reactions when these materials are exposed to moisture-contained molten salt [60]. Moisture reacts with fluorine ions, forming oxidants and highly corrosive hydrofluoric acid (HF) [9,27]:

$$H_2O(g) + 2F^- \rightarrow O^{2-} + 2HF(g) \quad (3)$$

Although O^{2-} itself is not oxidizing to metals, it influences corrosion by promoting the formation of oxide corrosion products [27]:

$$M + \frac{n}{2}O^{2-} \leftrightarrow MO_{\frac{n}{2}} + ne^- \quad (4)$$

where M denotes a metal element. The formed oxide corrosion product $MO_{\frac{n}{2}}$ can further dissolve in the fluoride salt through reaction with fluoride ions [27]:

$$MO_{\frac{n}{2}} + nF^- \leftrightarrow MF_n + \frac{n}{2}O^{2-} \quad (5)$$

The equilibrium potentials of electrochemical reactions in fluoride molten salt have been calculated for Ni, Fe, and Cr, and showing that Ni remains immune to corrosion at more positive potential than Fe and Cr. Cr has a broader oxide formation window than Ni, meaning that Cr_2O_3 can form at lower O^{2-} concentration compared to NiO [27]. Although Cr_2O_3 is thermodynamically more stable, the formation of a dense and protective oxide layer is generally unrealistic in molten fluorides, as Cr_2O_3 becomes porous due to its dissolution through the addition reaction in the molten salt [27].

It should be noted that high-temperature exposure itself can also

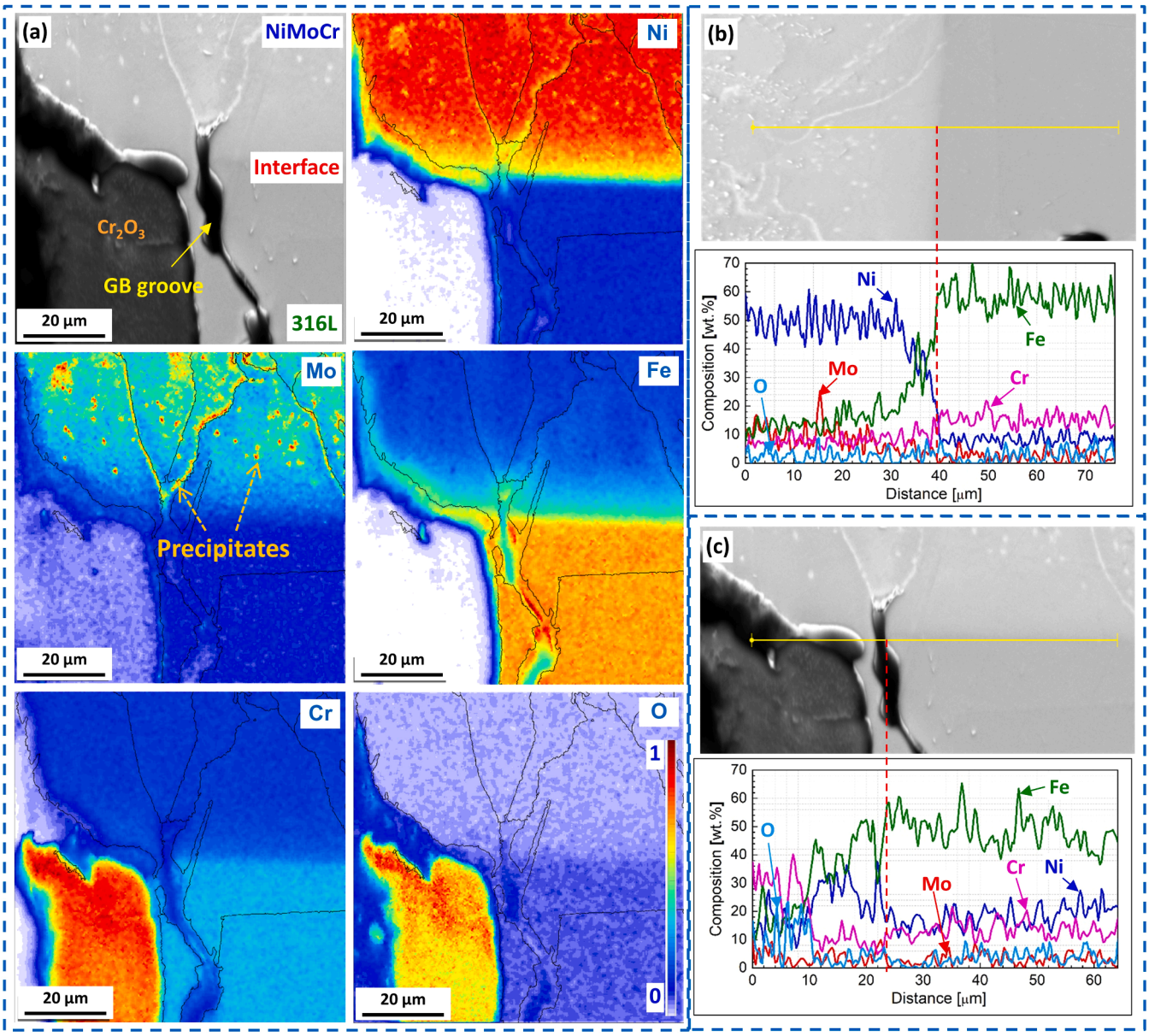


Fig. 11. Post-corrosion microstructural and compositional analyses of the transition region between the WAAM NiMoCr alloy cladding and the 316 L steel substrate. (a) SEM image and corresponding EDS elemental maps of Ni, Mo, Fe, Cr, and O, with an inset color legend in the O map indicating element levels, (b) EDS line scan perpendicular to the interface, and (c) EDS line scan parallel to the interface.

trigger microstructural evolution, such as diffusion-driven elemental redistribution and precipitation, even in the absence of molten salt. However, the observations described below (e.g., extensive Cr depletion, oxide formation, salt-filled grooves) require oxidizing species supplied by the molten salt environment and cannot be attributed to thermal exposure.

4.2.1. Intergranual corrosion of the steel substrate driven by Cr diffusion

The 316 L steel substrate undergoes severe corrosion after 500 h of exposure at 750 °C, leading to a residual corrosion-affected layer approximately 71 μm thick with deep grain boundary grooves (Fig. 6). SEM-EDS and TEM analyses (Figs. 7 and 8) confirm the predominant corrosion product as Cr_2O_3, supporting the oxidation-driven mechanism. While elevated temperature may promote some elemental diffusion in 316 L, the formation of Cr_2O_3 and the deep grain-boundary grooves clearly indicate reaction with oxidizing impurities in the molten salt rather than simple thermal aging.

The formation of surface Cr_2O_3 requires Cr migration from the bulk, either from grain interiors or along grain boundaries. This results in Cr-depleted zones, as evidenced by EDS line scans (Figs. 7b and 7c): Cr depletion extends ~5.3 μm into grain interiors and ~13.7 μm along grain boundaries. The magnitude and morphology of Cr depletion, together with oxide-filled grooves, strongly suggest chemically driven dealloying, which would not occur under thermal exposure alone. The latter value reflects a specific boundary analyzed in Fig. 7c, and longer boundaries may exhibit even greater depletion. Cr mapping (Fig. 7a) further reveals an interconnected depletion network along grain boundaries. These findings suggest that grain-boundary Cr depletion is the primary corrosion pathway for 316 L when galvanically coupled with NiMoCr in fluoride molten salt at 750 °C. This is consistent with the behavior of 316 L exposed to fluoride molten salt without coupling, where corrosion is likewise dominated by Cr dealloying and void formation along grain boundaries [10,61]. The absence of Cr segregation in the as-received microstructure (Fig. 1e) indicates that Cr must migration

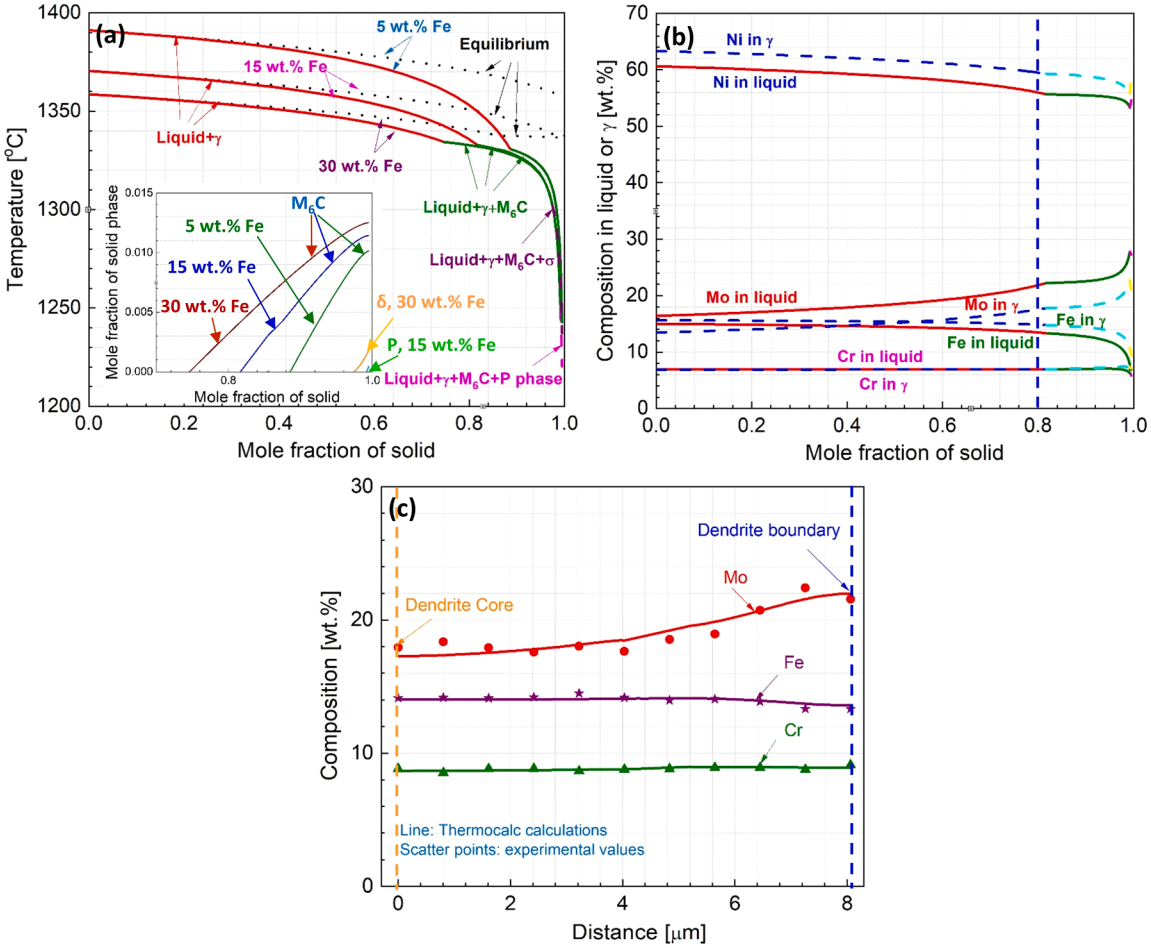


Fig. 12. Thermodynamic simulations of phase formation and elemental segregation in the WAAM NiMoCr alloy cladding. (a) Phase evolution during solidification of NiMoCr alloys with varying Fe contents (inset: magnified view of the mole fraction of solid phases), (b) elemental concentration in the liquid or γ-matrix phase as a function of solid mole fraction, and (c) comparison between simulated and experimental element distribution across a dendrite of 16.16 μm width.

via diffusion for its removal from the matrix and grain boundaries. Moreover, the increased stored energy and dislocation density near the grain boundaries, as suggested by elevated misorientation-to-mean and KAM values (Figs. 1c and 1d), indicate the presence of significant defects in these regions, which accelerate Cr diffusion and depletion along grain boundaries. Consequently, Cr diffusion plays a critical role in determining the corrosion rate of the steel substrate.

The diffusion coefficients of Cr in metallic materials can be estimated using the Arrhenius equation:

$$D = D_0 e^{-\frac{Q}{RT}} \tag{6}$$

where D_o is the pre-exponential factor, Q is the activation energy, R is the gas constant, and T is the temperature. For 316 L, the pre-exponential factor and activation energy are reported as 1.13×10^{-7} m^2/s and 234 kJ/mol for lattice diffusion, and 2.84×10^{-5} m^2/s and 90.6 kJ/mol for grain boundary diffusion [62]. Using these values, the diffusion coefficients for Cr in the 316 L substrate at 750 °C are calculated to be 1.27×10^{-19} m^2/s for lattice diffusion and 6.72×10^{-10} m^2/s for grain boundary diffusion. The grain boundary diffusion coefficient is approximately nine orders of magnitude higher than the lattice diffusion coefficient. This aligns with empirical evidence that grain boundaries in polycrystalline materials act as fast diffusion pathways with significantly enhanced atomic mobility. Consequently, the rapid grain boundary diffusion of Cr facilittates intergranual corrosion of the 316 L steel substrate in fluoride molten salt.

Additionally, because all specimens were tested together in a single crucible in this study, galvanic coupling between the NiMoCr clading and the 316 L substrate may have accurred [32]. Evidence of such interaction is seen in the Fe elemental map of the NiMoCr cladding (Fig. 9a), which shows Fe enrichment not only at the surface and within grain boundary grooves, but also within the γ-Ni matrix. In contrast, the Ni map of the 316 L substrate (Fig. 7a) reveals no significant Ni enrichment within the γ-Fe matrix, with Ni primarily located at the surface and along grain boundaries. The high concentrations of Fe and Ni in surface and groove regions are attributed to residual salt containing dissolved corrosion products. The presence of an Fe-enriched layer within the NiMoCr cladding suggests mass transfer of Fe from the steel substrate to the Ni alloy, likely driven by galvanic interaction. This behavior is consistence with findings from previous study involving Hastelloy N and 316 L couples in molten FLiNaK salt, where electrical contact led to galvanic corrosion. In that system, Hastelloy N acted as the cathode and 316 L as the anode, promoting steel corrosion and Fe migration to the Ni-based alloy [32]. A similar galvanic mechanism appears to have contributed to the accelerated degradation of the 316 L substrate and Fe enrichment in the NiMoCr cladding in the present study.

4.2.2. σ-phase formation and intradendritic corrosion in the NiMoCr alloy cladding

The WAAM NiMoCr cladding exhibits substantial Mo-enriched precipitate formation in the interdendritic regions after corrosion exposure (Fig. 9), in stark contrast to the as-fabricated microstructure (Fig. 2). High-temperature exposure alone can promote σ-phase precipitation in

Mo-rich Ni alloys; however, the preferential dissolution patterns observed at interdendritic sites confirm that molten-salt interactions also played a central role in driving the spatial corrosion behavior. This transformation indicates that the significant Mo segregation in interdendritic zones (Fig. 2) facilitates extensive dynamic precipitation during high-temperature corrosion at 750 °C for 500 h. Thermodynamic simulations (Fig. 13a), performed using the interdendritic composition at 750 °C, predict the volume fractions of various phases as a function of Mo content for varying Fe concentrations. In addition to the γ-matrix, the primary predicted precipitates are TCP σ-phase and a minor fraction of carbides, including M_6C, $M_{23}C_6$, and M_7C_3. Among these, $M_{23}C_6$ and M_7C_3 only form at relatively low Mo concentrations. One M_6C carbide was identified through TEM SAD patterns and EDS analysis (Fig. 10). As the Mo content increases, the volume fraction of σ-phase precipitates increases linearly, while that of M_6C carbides remains relatively constant and low, attributed to the low carbon content (0.05 wt%) in the NiMoCr alloy wire (Table 1). Furthermore, at a fixed Mo concentration, higher Fe content results in a greater volume fraction of σ-phase formation. Fig. 13b illustrates the simulated dynamic precipitation behavior of the σ-phase at 750 °C over a 500-hour exposure period. The number density of σ-phase precipitates increases rapidly, reaching ~4.81×10^{17} m^{-3} within just 0.0036 h, and gradually rises to a peak of ~5.06×10^{17} m^{-3} by 500 h, indicating rapid nucleation. These precipitates also exhibit substantial growth, reaching a radius of ~0.05 μm within 0.46 h. Continued growth occurs over longer exposure, with precipitates attaining a maximum size of ~0.6 μm and a peak volume fraction of ~0.24 after approximately 78.76 h. These results collectively suggest that the dynamically formed TCP σ-phase precipitates in the interdendritic regions influence the corrosion behavior of the WAAM cladding from the early stages of high-temperature exposure.

Despite the potential for galvanic coupling with the 316 L steel substrate, the NiMoCr alloy cladding, acting as the cathode, did not undergo severe degradation. The elemental depletion profiles (Fig. 9) further indicate active reaction with oxidizing species in the salt, distinguishing corrosion-driven changes from microstructural evolution caused solely by thermal exposure. Although Cr_2O_3 was not observed on the cladding surface, EDS analysis revealed noticeable depletion of key alloying elements, particularly Cr, followed by Ni and Mo (Fig. 9a). This suggests that degradation of the cladding can still occur due to residual oxidizing species in the salt, such as moisture, as described by reactions (3) - (5). Thermodynamic calculations (Fig. 13c) demonstrate that Mo content significantly affects the diffusion coefficients of key alloying elements at 750 °C. Specifically, increasing Mo content reduces the diffusion coefficient of Cr, while slightly increasing those of Fe and Ni. In conventionally fabricated NiMoCr alloys exposed to fluoride molten salt, Cr depletion drives intergranular corrosion [31]. In the WAAM NiMoCr alloy, Mo enrichment in interdendritic regions mitigates Cr loss and suppresses grain-boundary attack, thereby enhancing corrosion resistance in molten-salt environments.

During chemical processes such as etching or corrosion, precipitates can act as anodes, leading to their preferential dissolution relative to the matrix. This selective dissolution results in the formation of small pits, with their size directly related to the original precipitate size [63]. Conversely, if the precipitates have a higher electrochemical potential than the matrix, they can act as cathodic sites, promoting anodic dissolution of the surrounding matrix. This process may cause the precipitates to detach from the matrix due to undercutting, leading to significant material loss, particularly at grain boundaries. Severe intergranular corrosion has been observed in Hastelloy-N alloy containing M_6C carbides at grain boundaries when exposed to FLiNaK salts at 700 °C for 240 h [31]. In that case, the carbides acted as cathodes, while the adjacent substrate functioned as an anode, making the grain boundary regions particularly susceptible to corrosion and resulting in severe intergranular degradation [31]. However, in the present study

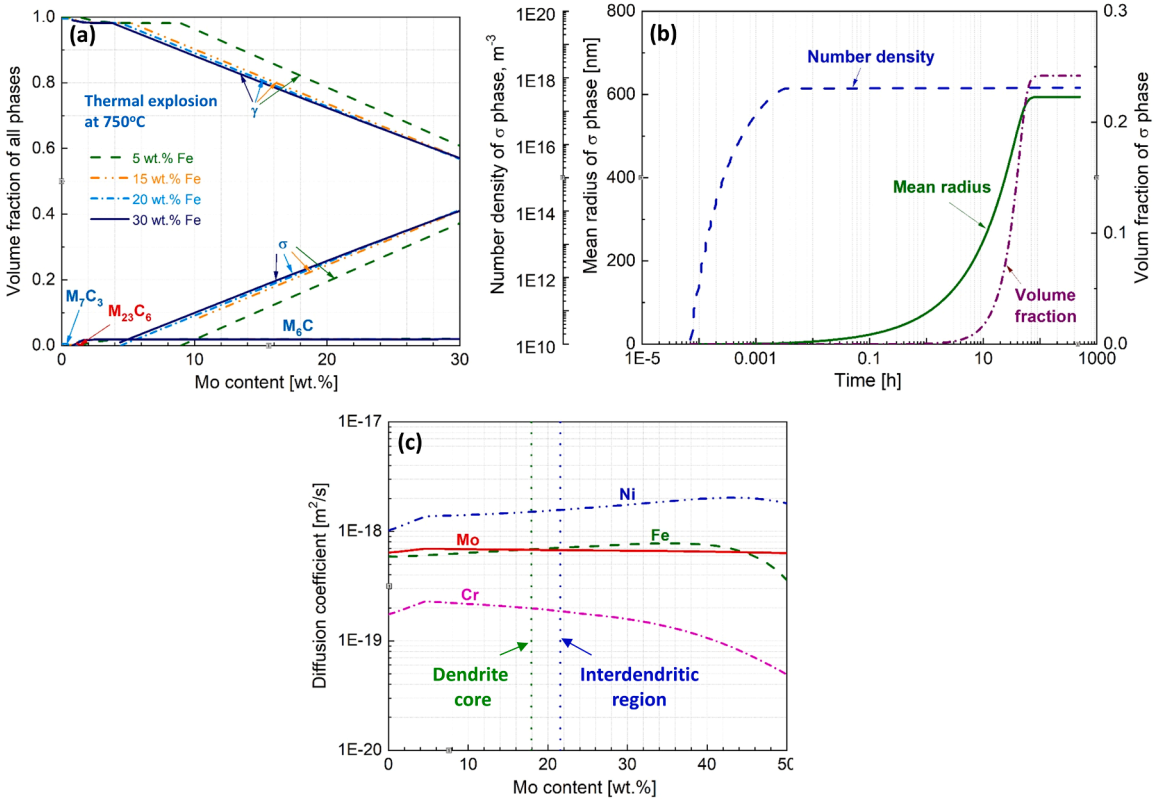


Fig. 13. Thermo-Calc simulations of precipitation behavior and elemental effects on diffusion and thermodynamic stability in the WAAM NiMoCr cladding and 316 L substrate at 750 °C. (a) Effect of Mo content on the equilibrium volume fraction of various phases in the NiMoCr cladding, (b) evolution of σ-phase number density, radius, and volume fraction in the NiMoCr cladding over 500 h, and (c) influence of Mo content on elemental diffusion coefficients in the NiMoCr cladding.

(Figs. 6 and 9), intradendritic corrosion is observed for the WAAM NiMoCr alloy, which contains a significant amount of TCP σ phase in the interdendritic region. However, this corrosion morphology again differs from changes expected from thermal exposure alone and reflects the combined influence of high-temperature diffusion and molten-salt chemistry. This suggests that the electrochemical potential difference between the σ phase precipitates and the matrix was significantly reduced due to severe Mo segregation in the interdendritic regions (Fig. 9). As a result, galvanic corrosion effects, leading to the preferential dissolution of either the σ phase precipitates or the matrix, were substantially diminished. Instead, the σ phase precipitates, which contain over 70 wt% Mo (Fig. 10b), demonstrated greater corrosion resistance than the surrounding interdendritic matrix. The post-corrosion microstructure (Figs. 6 and 9) shows that these precipitates remain in the front of the interdendritic region, indicating their superior corrosion resistance in the molten salt environment. Therefore, severe Mo segregation formed during WAAM processing and the dynamic precipitation of the TCP σ phase during high-temperature corrosion enhance the corrosion resistance of the interdendritic regions, ultimately resulting in intradendritic corrosion in the WAAM NiMoCr alloy cladding.

4.2.3. *Corrosion behavior of the transition region*

The corrosion behavior in the transition region between the WAAM NiMoCr alloy cladding and the 316 L steel substrate is governed by the combined influence of microstructural characteristics and compositional gradients. As shown in Figs. 3, 4, and 11, the as-fabricated microstructure contains carbides, while post-corrosion microstructures reveal dynamically formed σ-phase precipitates on the WAAM NiMoCr alloy side of the transition region. However, the precipitate density in this region is significantly lower than that observed in the dendritic regions (Fig. 11a), which can be attributed to its lower Mo content (Fig. 11a, Mo mapping, and Fig. 11b). Importantly, no Ni-Fe intermetallic phases were detected in the transition region, which minimizes galvanic coupling effects that could otherwise accelerate corrosion. In addition, the presence of CGGs and the absence of a sharp microstructural boundary between the steel substrate and the cladding reduces the defect accumulation, which in turn supresses the diffusion of Cr and other alloying elements, thereby mitigating corrosion rates.

EDS analysis of corroded samples (Fig. 11a) confirms that the transition region experiences significantly less corrosion than the bulk steel substrate. Intergranular corrosion initiates on the steel side due to rapid Cr depletion along grain boundaries, leading to the formation of Cr_2O_3 and the development of deep corrosion grooves (Fig. 11). However, these grooves do not extend beyond the transition zone. The presence of TCP-phase precipitates, along with a gradual decrease in Fe content and an increase in Mo concentration, stabilizes the FCC γ-phase and enhances its resistance to molten fluoride salt attack. Overall, the CGGs formed during deposition facilitate a gradual chemical and microstructural transition across the cladding-substrate intermaterial interface, which is not preferentially attacked, thereby enhancing the interface stability and structural integrity of the cladded system.

5. Conclusions

The microstructure and molten-salt corrosion behavior of WAAM-fabricated NiMoCr alloy cladded 316 L stainless steel were systematically investigated. Corrosion testing was performed at 750 °C for 500 h in eutectic FLiNaK salt using specimens extracted from the 316 L steel substrate, the NiMoCr alloy cladding, and the NiMoCr/316 L bistructure. All specimens were tested simultaneously in a single FLiNaK-filled crucible to simulate a worst-case scenario of galvanic interaction. Pre- and post-corrosion microstructural characterizations were correlated with the measured corrosion performance. The following conclusions can be drawn:

(1). Hierarchical grain structures developed in the WAAM NiMoCr alloy cladding, comprising < 001 > -textured columnar dendrites with significant Mo segregation and minor carbide formation in the interdendritic regions. At the cladding-substrate interface, CGGs formed, exhibiting continuous chemical and crystallographic transitions without a distinct boundary.

(2). Corrosion resistance varied across the sample types. The NiMoCr alloy cladding exhibited the lowest weight loss (5.67 mg/cm^2) and corrosion rate (0.11 mm/year), while the 316 L steel substrate showed the highest (12.92 mg/cm^2, 0.29 mm/year). The bistructure region demonstrated intermediate behavior (8.57 mg/cm^2, 0.18 mm/year), reflecting a gradual transition in corrosion performance. These results confirm that WAAM NiMoCr alloy cladding can effectively protect the underlying steel in high-temperature molten fluoride salt environments.

(3). Post-corrosion analyses revealed extensive Cr_2O_3 formation at the steel surface, indicating Cr depletion as the primary degradation mechanism. Rapid Cr diffusion along grain boundaries led to deep boundary grooves and pronounced intergranular corrosion. Galvanic coupling between the NiMoCr alloy cladding and the 316 L steel substrate further accelerated substrate degradation.

(4). In the NiMoCr alloy cladding, Mo segregation in the interdendritic regions suppressed Cr diffusion and promated the dynamic formation of corrosion-resistant σ-phase precipitates. These precipitates, along with the surrounding Mo-enriched γ-Ni matrix, mitigated galvanic interactions and shifted the corrosion mode from interdendritic to intradendritic.

(5). The CGGs in the transition zone provided an intermaterial interface that was not preferentially attacked, thereby improving interfacial stability and maintaining the overall structural integrity of the cladded system.

CRediT authorship contribution statement

Hanliang Zhu: Conceptualization, Formal analysis, Investigation, Methodology, Project administration, Visualization, Writing – original draft, Writing – review & editing. **Zhijun Qiu**: Investigation. **Zhiyang Wang**: Formal analysis, Investigation, Writing – review & editing. **Ondrej Muránsky**: Conceptualization, Formal analysis, Resources, Writing – review & editing. **Inna Karatchevtseva**: Investigation, Writing – review & editing. **Huijun Li**: Conceptualization, Project administration, Resources.

Declaration of Competing Interest

The authors declare that they have no known competing financial interests or personal relationships that could have appeared to influence the work reported in this paper.

Data availability

Data will be made available on request.

References

[1] J. Uhlíř, Chemistry and technology of molten salt reactors – history and perspectives, J. Nucl. Mater. 360 (1) (2007) 6–11.
[2] D. Hejazi, A.M. Alwafi, S.M. Alzahrani, M.M. Alqahtani, S.M. Alshehri, The small modular molten salt reactor potential and opportunity in Saudi Arabia, Nucl. Eng. Technol. 57 (2) (2025) 103203.
[3] D. LeBlanc, Molten salt reactors: a new beginning for an old idea, Nucl. Eng. Des. 240 (6) (2010) 1644–1656.
[4] F.-Y. Ouyang, C.-H. Chang, B.-C. You, T.-K. Yeh, J.-J. Kai, Effect of moisture on corrosion of Ni-based alloys in molten alkali fluoride FLiNaK salt environments, J. Nucl. Mater. 437 (1) (2013) 201–207.
[5] K.L. Murty, I. Charit, Structural materials for Gen-IV nuclear reactors: Challenges and opportunities, J. Nucl. Mater. 383 (1) (2008) 189–195.
[6] O. Muránsky, C. Yang, H. Zhu, I. Karatchevtseva, P. Sláma, Z. Nový, L. Edwards, Molten salt corrosion of Ni-Mo-Cr candidate structural materials for Molten Salt Reactor (MSR) systems, Corros. Sci. 159 (2019) 108087.
[7] L.C. Olson, J.W. Ambrosek, K. Sridharan, M.H. Anderson, T.R. Allen, Materials corrosion in molten LiF–NaF–KF salt, J. Fluor. Chem. 130 (1) (2009) 67–73.

[8] F.-Y. Ouyang, C.-H. Chang, J.-J. Kai, Long-term corrosion behaviors of Hastelloy-N and Hastelloy-B3 in moisture-containing molten FLiNaK salt environments, J. Nucl. Mater. 446 (1) (2014) 81–89.
[9] C. Yang, O. Muránsky, H. Zhu, I. Karatchevtseva, R. Holmes, M. Avdeev, Y. Jia, H. Huang, X. Zhou, Corrosion performance of Ni-16%wt.Mo-X%wt.SiC alloys in FLiNaK molten salt, Corros. Sci. 143 (2018) 240–248.
[10] H. Yin, J. Qiu, H. Liu, W. Liu, Y. Wang, Z. Fei, S. Zhao, X. An, J. Cheng, T. Chen, P. Zhang, G. Yu, L. Xie, Effect of CrF3 on the corrosion behaviour of Hastelloy-N and 316L stainless steel alloys in FLiNaK molten salt, Corros. Sci. 131 (2018) 355–364.
[11] M. Weinstein, C. Falconer, W. Doniger, L. Bailly-Salins, R. David, K. Sridharan, A. Couet, Environmental degradation of electroplated nickel and copper coated SS316H in molten FLiNaK salt, Corros. Sci. 191 (2021) 109735.
[12] G. Zheng, K. Sridharan, Corrosion of structural alloys in high-temperature molten fluoride salts for applications in molten salt reactors, JOM 70 (8) (2018) 1535–1541.
[13] Y. Wang, C. Falconer, A. Couet, Dendrite corrosion of 316L stainless steel weld joint in NaCl–MgCl2 molten salt loop, npj Mater. Degrad. 9 (1) (2025) 6.
[14] C.S. Sona, B.D. Gajbhiye, P.V. Hule, A.W. Patwardhan, C.S. Mathpati, A. Borgohain, N.K. Maheshwari, High temperature corrosion studies in molten salt-FLiNaK, Corros. Eng. Sci. Technol. 49 (4) (2014) 287–295.
[15] A. Morell-Pacheco, H. Kim, T. Wang, C.-H. Shiau, R. Balerio, A. Gabriel, L. Shao, Ni coating on 316L stainless steel using cage plasma treatment: feasibility and swelling studies, J. Nucl. Mater. 540 (2020) 152385.
[16] B. Wu, Z. Qiu, B. Dong, O. Muránsky, H. Zhu, Z. Wang, Z. Pan, H. Li, Microstructural characterisation and hardness assessment of wire arc cladded Hastelloy C276 on creep resistant steel P91, J. Mater. Res. Technol. 19 (2022) 3818–3827.
[17] L.Da. Silva Ferreira, K. Graf, A. Scheid, Microstructure and properties of nickel-based C276 alloy coatings by PTA on AISI 316L and API 5L X70 steel substrates, Mater. Res. 18 (1) (2015) 212–221.
[18] W.-Y. Chen, X. Zhang, M. Li, R. Xu, C. Zhao, T. Sun, Laser powder bed fusion of Inconel 718 on 316 stainless steel, Addit. Manuf. 36 (2020) 101500.
[19] R.K. Singh, K. Venkadeshwaran, B.P. Singh, G.K. Kantak, Assessing the pros and cons of wire-arc additive manufacturing for material production, Multidiscip. Rev. 6 (2024), 2023ss055.
[20] S. Jadhav, S. Kusekar, A. Belure, S. Digole, A. Mali, M. Cheepu, M. Mugale, S. Alkunte, D. Kim, Recent Progress and Scientific Challenges in Wire-Arc Additive Manufacturing of Metallic Multi-Material Structures, J. Manuf. Mater. Process. 9 (8) (2025) 284.
[21] S. Mohanty, K. Gokuldoss Prashanth, Metallic Coatings through Additive Manufacturing: A Review, Mater. (Basel) 16 (6) (2023) 2325.
[22] V. Lakkannavar, K.B. Yogesha, C.D. Prasad, R.K. Phanden, G. S, S.C. Prasad, Thermal spray coatings on high-temperature oxidation and corrosion applications – A comprehensive review, Results Surf. Interfaces 16 (2024) 100250.
[23] Z. Qiu, B. Wu, H. Zhu, Z. Wang, A. Hellier, Y. Ma, H. Li, O. Muransky, D. Wexler, Microstructure and mechanical properties of wire arc additively manufactured Hastelloy C276 alloy, Mater. Des. 195 (2020) 109007.
[24] Z. Qiu, H. Zhu, Z. Wang, O. Muránsky, T. Wei, E. Budzakoska-Testone, J. Davis, A. Studer, Q. Gu, U. Garbe, D. Wexler, H. Li, Crystallographic texture and multiscale boundaries mediated creep anisotropy in additively manufactured Ni-based Hastelloy C276 superalloy, Addit. Manuf. 83 (2024) 104069.
[25] C. Zhang, Z. Qiu, H. Zhu, Z. Wang, Z. Pan, J. Xi, H. Li, Microstructure and mechanical properties of bulked-wall Inconel 625 through wire and arc-based additive manufacturing, Prog. Addit. Manuf. 10 (9) (2025) 7155–7171.
[26] C. Zhang, Z. Qiu, H. Zhu, Z. Wang, O. Muránsky, M. Ionescu, Z. Pan, J. Xi, H. Li, On the Effect of Heat Input and Interpass Temperature on the Performance of Inconel 625 Alloy Deposited Using Wire Arc Additive Manufacturing–Cold Metal Transfer Process, Metals 12 (1) (2022) 46.
[27] S. Guo, J. Zhang, W. Wu, W. Zhou, Corrosion in the molten fluoride and chloride salts and materials development for nuclear applications, Prog. Mater. Sci. 97 (2018) 448–487.
[28] H. Zhu, R. Holmes, T. Hanley, J. Davis, K. Short, L. Edwards, High-temperature corrosion of helium ion-irradiated Ni-based alloy in fluoride molten salt, Corros. Sci. 91 (2015) 1–6.
[29] H. Zhu, R. Holmes, T. Hanley, J. Davis, K. Short, L. Edwards, Z. Li, Effects of bubbles on high-temperature corrosion of helium ion-irradiated Ni-based alloy in fluoride molten salt, Corros. Sci. 125 (2017) 184–193.
[30] W. Doniger, C. Falconer, A. Couet, K. Sridharan, Corrosion of 316L & 316H stainless steel in molten LiF-NaF-KF (FLiNaK), J. Nucl. Mater. 579 (2023) 154383.
[31] Y. Gu, W. Zhang, Y. Xu, Y. Shi, K. Volodymyr, Stress-assisted corrosion behaviour of Hastelloy N in FLiNaK molten salt environment, npj Mater. Degrad. 6 (1) (2022) 90.
[32] H. Sun, X. Ding, H. Ai, G. Lei, X. Yang, J.-Q. Wang, Interaction mechanisms of a Hastelloy N-316L stainless steel couple in molten LiF-NaF-KF salt, Corros. Sci. 164 (2020) 108317.
[33] Y. Wei, P. La, Y. Zheng, F. Zhan, H. Yu, P. Yang, M. Zhu, Z. Bai, Y. Gao, Review of Molten Salt Corrosion in Stainless Steels and Superalloys, Crystals 15 (3) (2025) 237.
[34] Z. Qiu, B. Dong, B. Wu, Z. Wang, K. Carpenter, T. Wu, J. Zhang, D. Wexler, H. Zhu, H. Li, Tailoring the surface finish, dendritic microstructure and mechanical properties of wire arc additively manufactured Hastelloy C276 alloy by magnetic arc oscillation, Addit. Manuf. 48 (2021) 102397.
[35] J.O. Andersson, T. Helander, L. Höglund, P. Shi, B. Sundman, Thermo-Calc & DICTRA, computational tools for materials science, Calphad Computer Coupling Phase Diagrams Thermochemistry 26 (2) (2002) 273–312.
[36] F. Bachmann, R. Hielscher, H. Schaeben, Texture analysis with MTEX- Free and open source software toolbox, Solid State Phenom. 160 (2010) 63–68.
[37] L.E. Murr, Metallurgy of additive manufacturing: Examples from electron beam melting, Addit. Manuf. 5 (2015) 40–53.
[38] N. Ishimatsu, Y. Kubo, N. Kitamura, N. Kawamura, S. Kawaguchi-Imada, T. Irifune, Elongation and compression of Fe-Fe atomic pairs in Fe-Ni invar alloys: Microscopic observations of the magnetovolume effect in ferromagnetic Fe-Ni fcc-based alloys, Phys. Rev. B 112 (6) (2025) 064109.
[39] H. Xu, Q. Liu, B. Leng, W. Zhang, X.-X. Ye, F. Han, X. Li, R. Liu, J. Wang, Non-uniform corrosion of UNS N10003 alloy induced by trace SO42- in molten FLiNaK salt, Corros. Sci. 192 (2021) 109802.
[40] Q. Liu, X. Liu, G. Hao, H. Xu, Effect of O2- additive on the corrosion behavior of Hastelloy N alloy in molten FLiNaK, Corros. Sci. 213 (2023) 111001.
[41] Q. Liu, B. Leng, J. Qiu, H. Yin, J. Lin, Z. Tang, Effect of graphite particles in molten LiF-NaF-KF eutectic salt on corrosion behaviour of GH3535 alloy, Corros. Sci. 168 (2020) 108581.
[42] W. Xue, X. Yang, Z. Li, X. Li, J. Wang, V. Ignatiev, X. Zhou, Effect of exposing duration on the interaction between nickel-based alloy and SiC in molten LiF-NaF-KF salt, J. Nucl. Mater. 515 (2019) 276–283.
[43] K.M. Sankar, P.M. Singh, Effect of Li metal addition on corrosion control of Hastelloy N and stainless steel 316H in molten LiF-NaF-KF, J. Nucl. Mater. 555 (2021) 153098.
[44] C.S. Sona, B.D. Gajbhiye, P.V. Hule, A.W. Patwardhan, C.S. Mathpati, A. Borgohain, N.K. Maheshwari, High temperature corrosion studies in molten salt-FLiNaK, Corros. Eng. Sci. Technol. 49 (4) (2014) 287–295.
[45] M. Lee, O. Muránsky, I. Karatchevtseva, H. Huang, K.J. Laws, Corrosion performance of Ni-based structural alloys for applications in molten-salt based energy systems: Experiment & numerical validation, Corros. Sci. 190 (2021) 109607.
[46] A.E. Danon, O. Muránsky, I. Karatchevtseva, Z. Zhang, Z.J. Li, N. Scales, J. J. Kruzic, L. Edwards, Molten salt corrosion (FLiNaK) of a Ni–Mo–Cr alloy and its welds for application in energy-generation and energy-storage systems, Corros. Sci. 164 (2020) 108306.
[47] O. Muránsky, I. Karatchevtseva, A.E. Danon, R. Holmes, P. Huai, Z. Zhang, Impact of dislocations and dislocation substructures on molten salt corrosion of alloys under plasticity-imparting conditions, Corros. Sci. 176 (2020) 108915.
[48] X.-X. Ye, H. Ai, Z. Guo, H. Huang, L. Jiang, J. Wang, Z. Li, X. Zhou, The high-temperature corrosion of Hastelloy N alloy (UNS N10003) in molten fluoride salts analysed by STXM, XAS, XRD, SEM, EPMA, TEM/EDS, Corros. Sci. 106 (2016) 249–259.
[49] R.H. Banerjee, V. Singh, P. Chakraborty, V. Karki, G. Abraham, R. Tewari, Investigating Cr dealloying and Li ingress in Ni-Mo-Cr alloys with different Mo/Cr ratio exposed to FLiNaK salt, Corros. Sci. 212 (2023) 110929.
[50] A. Ramu, V. Pavlik, V. Sillikova, M. Boca, Corrosion Behavior of Incoloy®800H, Hastelloy®G35® and 316L Stainless Steel in the Molten Eutectic Fluoride Mixture FLiNaK and Its Vapors, Materials 16 (7) (2023) 2679.
[51] Q. Liu, H. Sun, H. Yin, L. Guo, J. Qiu, J. Lin, Z. Tang, Corrosion behaviour of 316H stainless steel in molten FLiNaK eutectic salt containing graphite particles, Corros. Sci. 160 (2019) 108174.
[52] K.K. Sandhi, J. Szpunar, Analysis of Corrosion of Hastelloy-N, Alloy X750, SS316 and SS304 in Molten Salt High-Temperature Environment, Energies 14 (3) (2021) 543.
[53] R.S. Sellers, C. Wei-Jen, K.B. C, A.M. H, S. Kumar, W. Chaur-Jeng, T.R, Allen, Corrosion of 316L Stainless Steel Alloy and Hastelloy-N Superalloy in Molten Eutectic LiF-NaF-KF Salt and Interaction with Graphite, Nucl. Technol. 188 (2) (2014) 192–199.
[54] Y. Yang, J.T. Busby, Thermodynamic modeling and kinetics simulation of precipitate phases in AISI 316 stainless steels, J. Nucl. Mater. 448 (1) (2014) 282–293.
[55] Z. Qiu, B. Wu, Z. Wang, D. Wexler, K. Carpenter, H. Zhu, O. Muránsky, J. Zhang, H. Li, Effects of post heat treatment on the microstructure and mechanical properties of wire arc additively manufactured Hastelloy C276 alloy, Mater. Charact. 177 (2021) 111158.
[56] C.M.F. Rae, R.C. Reed, The precipitation of topologically close-packed phases in rhenium-containing superalloys, Acta Mater. 49 (19) (2001) 4113–4125.
[57] H. Zhu, Y. Ma, T. Wei, H. Li, R. Aughterson, G. Lumpkin, The formation and Kr-ion irradiation behaviour of new microstructural features in additively manufactured titanium aluminium alloy, Addit. Manuf. 29 (2019) 100766.
[58] H. Zhu, Z. Wang, O. Muránsky, J. Davis, S. Yu, D. Kent, G. Wang, M.S. Dargusch, The characterisation and formation of novel microstructural features in a Ti−Nb−Zr−Mo−Sn alloy manufactured by Laser Engineered Net Shaping (LENS), Addit. Manuf. 37 (2021) 101705.
[59] Y. Wang, H. Liu, C. Zeng, Galvanic corrosion of pure metals in molten fluorides, J. Fluor. Chem. 165 (2014) 1–6.
[60] S. Delpech, C. Cabet, C. Slim, G.S. Picard, Molten fluorides for nuclear applications, Mater. Today 13 (12) (2010) 34–41.
[61] L. Olson, K. Sridharan, M. Anderson, T. Allen, Intergranular corrosion of high temperature alloys in molten fluoride salts, Mater. High. Temp. 27 (2) (2010) 145–149.
[62] M. Mizouchi, Y. Yamazaki, Y. Iijima, K. Arioka, Low temperature grain boundary diffusion of chromium in SUS316 and 316L stainless steels, Mater. Trans. 45 (10) (2004) 2945–2950.
[63] H. Zhu, Etching behavior of aluminum alloy extrusions, JOM 66 (11) (2014) 2222–2228.